Synchronization for Impulse Radio Ultra-Wideband System

CAO RUI

(B.Eng. Zhejiang University)

A THESIS SUBMITTED

FOR THE DEGREE OF MASTER OF ENGINEERING

DEPARTMENT OF ELECTRICAL AND COMPUTER

ENGINEERING

NATIONAL UNIVERSITY OF SINGAPORE

2005

ACKNOWLEDGEMENT

I would like to take this opportunity to express my deepest appreciation to my supervisors Dr. Zheng Yuanjin (IME) and Prof. Lian Yong (NUS). They led me to this totally new domain and showed me the beauty of a logic world.

I would also like to thank my father, Prof. Cao Tingbin, who taught me $1+1=2$ and $E=mc^2$.

I would like to thank Mr. Kong Zhuqing as well, my high school physics lecturer, who told me the words, ‘Philosophy is the Science of all sciences’.

Many thanks to my co-workers Miss Zou Xiaodan and Miss Ng Jia Hui, for their supportive work.

Also, I would share the joy of my achievement with my family. They have always been there for me no matter what comes up.

Finally, my friends here in the Singapore, Miss Wei Xiaoqian, Mr. Pu Yu, Mr. Tong Yan, Miss He Ying, Miss Yan Jiangnan, Mr. Cao Mingzheng, Miss Yang Liu, Miss Zhou Qiaoer, I would like to say ‘thanks for being there’.

TABLE OF CONTENT

SUMMARY

Ultra-Wideband (UWB) communication systems provide better performance over conventional wireless communication schemes. Traditionally, RAKE receivers are adopted in UWB receiver to explore rich multi-path components incorporated in the received signal. To improve the performance of a RAKE receiver, two approaches are frequently employed. The first one is to increase the transmitted signal energy, which leads to better performance, but consumes more power. The second one is to capture as much as possible energy in the received signal which achieves better performance without increasing the transmitted pulse energy.

In this thesis, a new synchronization scheme based on an efficient detector is proposed. It is shown by performance analysis and simulation that the proposed scheme outperforms traditional schemes.

With the improved synchronization algorithm, a new RAKE receiver structure is constructed and analyzed theoretically. The new RAKE structure synchronizes each finger with the proposed synchronization scheme. The theoretical performance shows that with the same input, the new RAKE receiver performs better than conventional ones.

LIST OF FIGURES

LIST OF SYMBOLS AND ABBREVIATIONS

UWB	Ultra-Wideband
EM	Electrical Magnetic
LTI	Linear Time Invariant
FCC	Federal Communications Commission
MB-UWB	Multi-Band UWB
DS-UWB	Direct Sequence UWB
AWGN	Additive White Gaussian Noise
ML	Maximum-Likelihood
MAP	Maximum A Posteriori Probability
PDF	Probability Density Function
i.i.d.	Identical Independent Distributed
R.V.	Random Variable
SNR	Signal Noise Ratio
MF	Matched Filter
SS	Spread Spectrum
CDMA	Code Division Multi-Access
GPS	Global Positioning System
DSSS	Direct Sequence Spread Spectrum
THSS	Time Hopping Spread Spectrum
IR	Impulse Radio

PN	Pseudo-Noise
S-V	Saleh-Valenzuela Channel Model
DLL	Delay Lock Loop
LOS	Line of Sight
GLRT	Generalized Likelihood Ratio Test
MRC	Maximum Ratio Combining
T&L	Trigg and Leach
CFAR	Constant False Alarm Rate
ARMA	Auto Regressive Moving Average
LPF	Low Pass Filter
VCO	Voltage Controlled Oscillator
LNA	Low Noise Amplifier
WSS	Wide Sense Stationary
MSE	Mean Square Error
MMSE	Minimum Mean Square Error
LMS	Least Mean Square
ROC	Receiver Operation Character

$r(t)$	Received Signal
$s(t)$	Transmitted Signal
$n(t)$	AWGN before Correlation
f_c	Carrier Frequency
τ_i	Path Delay of the i^{th} Path
$\tilde{\tau}_i$	The Estimator of τ_i
γ_i	Path Attenuation of the i^{th} Path
$\tilde{\gamma}_i$	The Estimator of γ_i
N_0	AWGN Single Side Power
Λ	Likelihood Function
$h(t)$	Channel Impulse Response
$\delta(t)$	Dirac Delta Function
ζ_i	SNR at the i^{th} Branch of RAKE
E_b	Bit Energy
E_p	Pulse Energy
$a(n)$	Pulse Amplitude of the n^{th} Frame
$b(n)$	PPM Bit Information of the n^{th} Frame
N_p	Number of Pulses with the Same information
T_f	Pulse Repetition Time
N_c	Chip Numbers within a Frame
T_c	Width of Each Chip

N_f	Code Length of the PN Code
$\left\{c^{(u)}(n)\right\}$	PN Code of the u^{th} user for PPM
$\left\{c_{DS}^{(u)}(n)\right\}$	DS Code of the u^{th} user for BPSK
Δ	Position Off-set for PPM
$p(t)$	Pulse Wave Form
$p_G(t)$	Gaussian Monocycle Function
T_p	Pulse Duration
P_{fa}	False Alarm Probability
P_d	Detection Probability
P_e	Error Probability
λ	Threshold Value
$\varepsilon(n)$	The T&L Detector Input
$e_f(n)$	The Numerator Branch of T&L Detector
$e_a(n)$	The Denominator Branch of T&L Detector
$x_{fa}(n)$	The Output of T&L Detector
ρ	Forgetting Factor of the ARMA Process
L_p	Number of Multi-paths
L_c	Number of Correctly Captured Paths
L_e	Number of Incorrectly Captured Paths
T	Multi-path Delay Vector
$\tilde{\mathrm{T}}$	Estimation of Multi-path Delay Vector
Γ	Multi-path Fading Vector

$\tilde{\Gamma}$	RAKE Fingers Vector
$X(n)$	RAKE Correlation Band Output Vector
$d(n)$	Desired Symbol
$\xi(n)$	Cost Function
$R_p(\Delta)$	Auto-Correlation Function of the Pulse
$w(n)$	Additive Noise after Correlation
σ_w^2	Noise Power After Correlation
$Q(x)$	Right Tail Accumulative Function
G	Processing Gain
H_0	Hypothesis that synchronization is not achieved
H_1	Hypothesis that synchronization is achieved
$f_{X_{fa}}(x_{fa})$	The PDF of T&L output
$f_{e_f}(e_f)$	The PDF of the numerator of T&L Detector
$f_{e_a}(e_a)$	The PDF of the denominator of T&L Detector
μ_ε	The Mean of T&L Input $\varepsilon(n)$
μ_τ	The Mean of $\left\|\varepsilon(n)\right\|$
μ_{e_f}	Mean of the numerator of T&L Detector
μ_{e_a}	Mean of the denominator of T&L Detector
$f_\tau(x)$	The Distribution of $\left\|\varepsilon(n)\right\|$
$P_G(\tilde{T})$	The Receiver Local Pulse Template
$y(n)$	RAKE Output
$e(n)$	Error between $d(n)$ and $y(n)$

1 INTRODUCTION

1.1 Introduction of IEEE 802.15.3a

In the recent decades, wireless technologies become more and more popular. Various wireless communication schemes are developed for higher transmission rate. Generally, there are two categories of communication schemes, namely carrier based and non-carrier based.

Carrier based systems are very popular. For example, IEEE 802.11g wireless local area network (Wireless LAN) aims at up to 54Mbps and ideal transmission distance of 1000ft. Another similar example is the famous BlueTooth wireless communication system which is dedicated for short range (less than 10m), low data rate (less than 1Mbps) wireless communications between portable devices such as laptops and cellular phones. The typical bandwidth of these systems is much smaller than their carrier frequencies. For instance, IEEE 802.11g occupies the maximum bandwidth of 108MHz (2×54MHz) centered at 2400MHz.

The transmission is satisfactory, as long as a frequency non-selective channel is encountered. However the situation may change as soon as destructive channel fading appears. One important concept is the coherent bandwidth [2] which is defined as the channel bandwidth within which the transmitted signal suffers from almost the same channel attenuation. A typical coherent channel bandwidth is several dozen mage Hertz [2] which is comparable to the narrowband. Thus narrowband systems are prone to be vulnerable to destructive channel fading.

To improve the reliability of transmissions over a fading channel, diversity techniques are frequently used. Signal is transmitted over different channels in either time or frequency domain which suffers from uncorrelated channel attenuations. Received signals, collected from different channels, are combined together with optimum coefficients by applying appropriate criterion, e.g. maximum ratio combining (MRC) [2]. The essence is that by transferring the same information through different channels, the risk that all received signal replicas are severely distorted is reduced significantly. Multiple inputs multiple outputs for spatial diversity and RAKE receiver for time domain diversity are two typical examples.

Ultra-Wideband (UWB) technology follows the same rationale.

As early as 19th century, research on wide-band signal for communications has been started followed the discovery of electrical magnetic (EM) field. The EM pulse is naturally a broad-band signal. However, the bandwidth is not controllable at that stage. In the 1960s', the origin of UWB emerged (Dr. Ross 1963, 1966) in the study of time-domain transient channel behavior which is an alternative way of channel characterization. The concept is quite simple, instead of characterizing a linear time-invariant (LTI) system by measuring its response to a batch of single tones, time domain measurements of the response to an impulse could also fully characterize the LTI system [3], [55].

UWB technology has found its applications in the military for decades. It is often referred to as "carrier-less short pulse" techniques [4]. The revived interest in UWB technology for civil utilization comes along with the growing interest in higher data rate and lower power consumption portable devices. A widely adopted definition of a UWB system is that any radio or wireless devices where the occupied bandwidth is greater than 500MHz [5]. Federal Communications Commission (FCC) has recently allowed unlicensed usage between the frequencies 3.1GHz and 10.6GHz. The FCC frequency mask is shown in Figure 1.1. The upper limit of the transmission power is -41.3dBm for indoor usage.

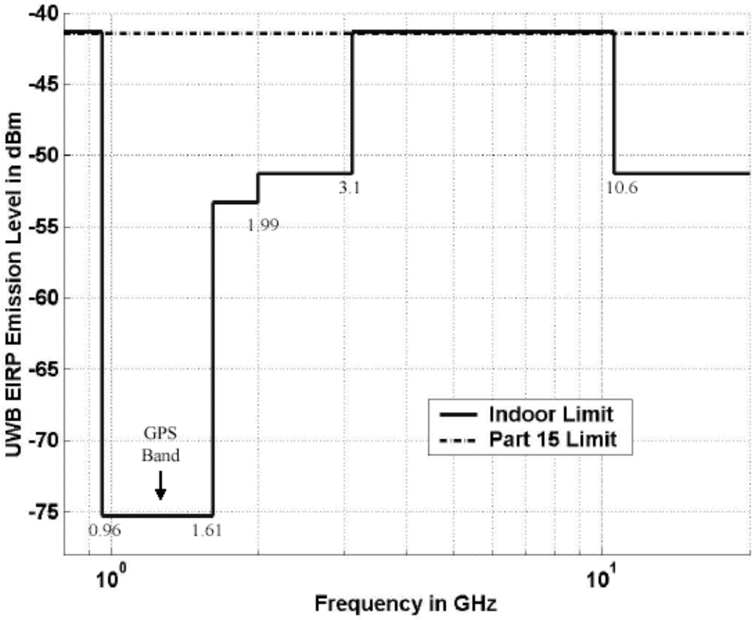

Figure 1.1 FCC frequency mask for UWB bandwidth.

To utilize the UWB bandwidth, two different schemes emerged, namely Multi-Band UWB (MB-UWB) and Direct Sequence UWB (DS-UWB). Each scheme attracted several advocators, and each has its own advantages and drawbacks. Multi-band techniques have already been developed successfully for decades, and MB-UWB supporters wish to utilize the existing techniques so as to reduce their cost. While DS-UWB is better in that it has a relatively simple transceiver structure. The impulse nature and ultra-wide bandwidth of DS-UWB make it a viable candidate for communications in dense multi-path environments (e.g. the typical office environment) because of its fine delay resolution properties [4].

However, the impulse nature indicates the extremely short pulse width comes along with the ultra-wide bandwidth. Usually, the pulse width is at sub-nanosecond order (typically 0.1ns~1ns). In comparison with the pulse repetition time (typically 10ns, for 100Mbps data rate), the duty cycle is much smaller than 1%. This means the pulse only exists in a relatively shot period during one cycle. The timing uncertainty to be solved is a great challenge. This is how the synchronization problem aroused.

A delicately designed RAKE receiver is usually employed to explore the rich multi-path components and gives optimum decisions on the transmitted information.

1.2 Introduction of Synchronization

To analyze the synchronization problem, the following received signal model is usually adopted

$$r(t) = s(t-\tau) + n(t), \tag{1.1}$$

where $s(t)$ is the transmitted signal. For a carrier based system, $s(t) = \mathrm{Re}\left[s_l(t)e^{j2\pi f_c t}\right]$, where $s_l(t)$ represents the equivalent low-pass signal, and the carrier frequency is f_c. While for a carrier-less system, the signal $s(t)$ is a sequence of pulses which fit into the transmission band naturally. $n(t)$ is the additive white Gaussian noise (AWGN), with two side power density $N_0/2$, τ corresponds to the propagation delay.

Most communication systems are based on the optimum receiver structure which is elaborated in [2]. To extract the information from the received signals, the receiver should acquire correct timing information before demodulating. As long as a carrier based system is concerned, synchronization is to eliminate the phase error between the carrier of the received signal and local carrier (it could be either an oscillator or a matched filter). While for a carrier-less system, e.g. a DS-UWB system, the timing information is the delay error between the received pulse and the local pulse template.

There are two widely applied criterions for signal parameter estimation, namely the maximum-likelihood (ML) criterion and the maximum a posteriori probability (MAP) criterion [2].

To apply the ML criterion, a likelihood function based the probability density function (PDF) $p(r|\tau)$ parameterized by the estimated propagation delay τ is constructed,

$$\Lambda(\tilde{\tau}) = \exp\left\{ -\frac{1}{N_0} \int_0^{T_f} \left[r(t) - s(t;\tilde{\tau}) \right]^2 dt \right\}. \tag{1.2}$$

The signal parameter, $\tilde{\tau}$ is treated as deterministic but unknown [2]. The estimated signal parameter is

$$\tilde{\tau}_{ML} = \underset{\tilde{\tau}}{\operatorname{argmax}} \left(\Lambda(\tilde{\tau}) \right). \tag{1.3}$$

To apply the MAP criterion, the PDF to be maximized is

$$p(\tau|r) = \frac{p(r|\tau)\, p(\tau)}{p(r)} \tag{1.4}$$

Equation (1.4) is also know as the Bayesian probability function. Unlike the likelihood function in equation (1.2) which assume the parameter $\tilde{\tau}$ a deterministic value, equation (1.4) is based on the pre-knowledge of the τ distribution.

Once synchronization is achieved, the receiver proceeded to the next stage, the data detection.

1.3 Introduction of RAKE Receiver

In the real world, besides the AWGN contamination, transmitted signal also suffers from severe channel attenuation as the electromagnetic (EM) wave traveling through the media. There are channel effects as deflections, reflections and scattering to the EM waves before the signal can reach the receiver. To simplify the analysis, a multi-path fading channel model is usually employed

$$h(t) = \sum_{i=0}^{L_p} \gamma_i \delta(t - \tau_i), \tag{1.5}$$

where $\delta(t)$ is the Dirac delta function, and γ_i and τ_i are the channel attenuation and the propagation delay of the i^{th} path of the total L_p paths respectively. Usually for $L_p \to \infty$, $\sum_{i=0}^{L_p} \gamma_i^2 = 1$ is assumed. γ_i is usually modeled as an identical independent distributed (i.i.d.) random variable (RV). The most frequently investigated distributions are Rayleigh, Rice, Nakagami *m* and Lognormal distributions, depending on channel that is involved in the transmission.

Thus, instead of (1.1), received signal modeled as

$$r(t) = \sum_{i=0}^{L_p} \gamma_i s(t - \tau_i) + n(t) \tag{1.6}$$

is employed to analyze the receiver functionality and performance. This expression indicates that the signal energy is dispersed by different multi-path components. To reconstruct the transmitted signal, RAKE structure [2], as shown in Figure 1.2, is employed to collect signal energy dispersed in different multi-path components. Usually, for each one channel realization, the channel fading coefficients γ_i are considered deterministic and constant.

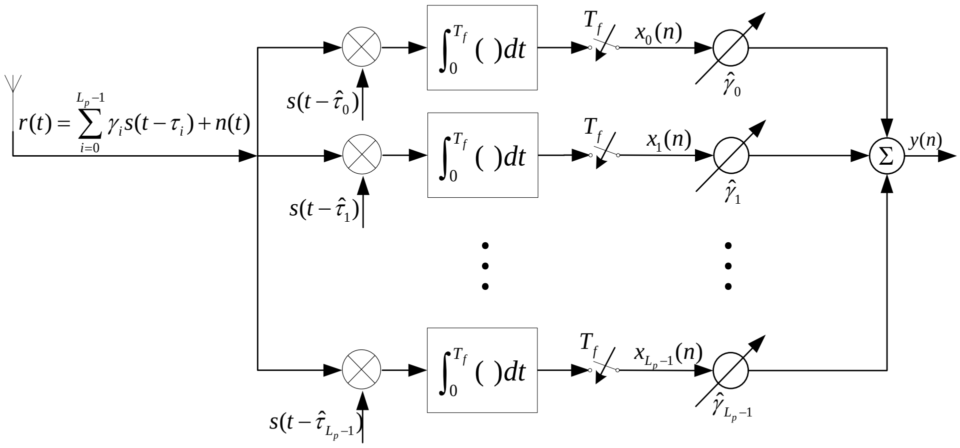

Figure 1.2 RAKE Receiver Structure.

Ideally, the SNR at the output of the RAKE receiver is [2]

$$\zeta_b = \frac{E_b}{N_0/2}\sum_{i=1}^{L_p}\gamma_i^2 \tag{1.7}$$

with the assumption $\sum_{i=0}^{L_p}\gamma_i^2 = 1$, the output (1.7) recovers the received signal to the largest possible SNR. While for a single branch matched filter (MF) or correlation receiver, the output SNR is on average

$$\bar{\zeta}_i = \frac{E_b}{N_0/2}E\left\{\gamma_i^2\right\} \tag{1.8}$$

where $E\{x\}$ is the expectation of RV x.

RAKE receiver is an implementation of exploring time domain diversity.

1.4 Scope of the Whole Project

This project was a part of the Agency of Science Technology and Research (A-STAR) UWB Research program, collaborating between the Institute of Microelectronics, Singapore and the National University of Singapore.

The whole project was targeted at prototyping an IEEE 802.15.3a transceiver based on DS-UWB scheme. Several sub-projects were split from the large project, including the one described in this thesis.

The main target of this project was to develop a fast and efficient synchronization algorithm for the DS-UWB scheme. Performance analysis was carried out to evaluate the algorithm. The theoretic results were then compared with the simulation results to verify the performance analysis.

After that, a RAKE structure which employed the proposed synchronization algorithm was also constructed. The performance analysis was then carried out. Unlike conventional analysis which assumes perfect synchronization, the performance analysis in this thesis was more close to a practical situation, an imperfect synchronization scenario. The performance analysis of the RAKE receiver was combined with the synchronization algorithm. This gave an overview of how the RAKE receiver works in the real world.

The hardware implementation problem was also involved in this project.

1.5 The Organization of this Thesis

The organization of this thesis is presented as follows.

In Chapter 2, the literature review of UWB systems is addressed. Literature include a brief introduction of spread spectrum system, a concrete review of UWB systems and a unique algorithm that may potentially improve the detection performance.

In Chapter 3, the proposed detector for impulse radio UWB system is presented in detail. Each sub-block is elaborated and the behavior of the detector is presented by simulation.

In Chapter 4, the RAKE receiver structure based on the proposed T&L synchronization algorithm is constructed. Its behavior is examined by simulation.

The performance analysis of the proposed synchronization algorithm and the new RAKE receiver structure are addressed in Chapter 5. Better performance is proved mathematically in this chapter.

Simulation results are shown and discussed in Chapter 6.

In Chapter 7, some hardware implementation issues are discussed.

Finally, the thesis is concluded in Chapter 8.

A new synchronization algorithm is proposed and a new RAKE structure is constructed which are both proved to perform better than conventional ones.

2 LITERATURE REVIEW

2.1 Review of Spread Spectrum (SS) Communication

The conventional carrier based communication systems transmit signals in a relatively narrowband. However, as mentioned in the Section 1.1, narrowband signal is vulnerable to severely destructive channel fading. To ensure the success of the communication over the frequency selective fading channels, frequency diversity technique is often adopted. The essence of this technique is to transmit the same information over a broadened bandwidth rather than using a single tone. By exploring the intrinsic frequency diversity in the received signals, tremendous gain is expected.

Shannon theory gives the elegant theoretical explanation to the truth stated above.

$$C = 1.44W \ln\left(1 + SNR\right) \tag{2.1}$$

where C is the channel capacity (bit/s), W is the channel bandwidth, SNR is the signal-to-noise ratio. The rationale is that at certain SNR, the channel capacity is proportional to the channel bandwidth W. At a fixed SNR, broader bandwidth is necessary for better performance.

Classical code division multi-access (CMDA) systems follow the same rationale. For instance, in GPS-L1 (1575.42MHz) system which transmits information at 50bits/s, the signal bandwidth is extended to 2.046MHz by multiplying a set of pseudo-noise (PN) code to the information modulated carrier. This can provide a processing gain of 30dB compared to the original signal.

The GPS system is a typical example of direct sequence spread spectrum (DSSS) systems. Some other spread spectrum (SS) systems are also investigated in the past decades. They are time hopping spread spectrum (THSS), frequency hopping spread spectrum (FHSS), FH-TH hybrid systems, and TH-DS hybrid systems, etc.[6]

DS-UWB, unlike conventional SS systems, spreads the signal bandwidth with ultra-wideband pulses. This unique characteristic distinguishes DS-UWB clearly from other carrier-based communication systems. Detailed description is in the following section.

2.2 Review of UWB Communication

2.2.1 How it works?

The DS-UWB system which transmits information via very narrow pulses is categorized as impulse radio (IR) system [7]. Because no carrier is involved in the communication, it is also referred to as a carrier-less communication system. The transmitted signal of the u^{th} user is [8]

$$s^{(u)}(t)=\sqrt{E_p}\sum\nolimits_{n=-\infty}^{+\infty}a^{(u)}\left(\left\lfloor n/N_p\right\rfloor\right)\cdot c_{DS}^{(u)}\left(n\right)\cdot p\left(t-nT_f-c^{(u)}\left(n\right)T_c-b^{(u)}\left(\left\lfloor n/N_p\right\rfloor\right)\Delta\right)\tag{2.2}$$

where E_p is the pulse energy at the transmitter end, $a(n)$ is the pulse amplitude at the n^{th} time instance, to increase SNR at the receiver end, N_p replicas are transmitted consecutively. T_f is pulse repetition time which is also the duration of a frame. Each frame is divided into N_c chips with chip duration T_c. $\left\{c^{(u)}(n)\right\}$ is the PN code of the u^{th} user and is repeated every other N_f pulses. $\left\{c_{DS}^{(u)}\left(n\right)\right\}$ stand for the users' specified direct sequence code with the length of N_f. Specifically, each N_f pulses consist a symbol. For sake of simplicity, $N_f = N_p$ is usually presumed. This assumption is presumed all through this thesis. The signal $b(n)$ corresponds to the pulse shift with respect to non-data modulated position. The pulse position shift is Δ when $b(n)$ is none zero. The pulse waveform is denoted by $p(t)$.

For PAM and BPSK signals, $b(n) = 0$, and $a(n)$ represents the transmitted information.

$$s^{(u)}(t) = \sqrt{E_p} \sum_{n=-\infty}^{+\infty} a^{(u)}\left(\left\lfloor n/N_f \right\rfloor\right) \cdot c_{DS}^{(u)}(n) \cdot p\left(t - nT_f\right). \tag{2.3}$$

For PPM signals, $a(n) = 1$, and $b(n)$ represents the transmitted information.

$$s^{(u)}(t) = \sqrt{E_p} \sum_{n=-\infty}^{+\infty} p\left(t - nT_f - c^{(u)}(n) T_c - b^{(u)}\left(\left\lfloor n/N_f \right\rfloor\right)\Delta\right). \tag{2.4}$$

There may also be some other hybrid modulation schemes depending on different realizations.

The signal then travels through the multi-path fading channel, and is contaminated by AWGN. The received signal could be represented as

$$r^{(u)}(t) = s^{(u)}(t) \otimes h(t - \tau_0) + n(t) \tag{2.5}$$

where $n(t)$ is AWGN with two sides power spectrum density $\frac{N_0}{2}$.

$h(t)$ is the impulse response of the channel, τ_0 is the propagation delay of the first arrival ray (usually the line of sight (LOS) path). Several channel models have been proposed so far based on different measurements [9], [10], [43]-[49]， in response to call for IEEE 802.15.3a indoor application. The most frequently employed channel model is a modified Saleh-Valenzuela (S-V) model [9], which is [10],

$$h_j(t) = X_j \sum_{l=0}^{L-1} \sum_{k=0}^{K-1} \alpha_{k,l}^{j} \delta(t - T_l^j - \tau_{k,l}^j), \tag{2.6}$$

where $\left\{\alpha_{k,l}^{j}\right\}$ is the multipath gain coefficients with log-normal distribution, $\left\{T_l^{j}\right\}$ is the delay of the l^{th} cluster, $\left\{\tau_{k,l}^{j}\right\}$ is the delay of the k^{th} multipath component relative to the l^{th} cluster arrival time T_l^{j}, $\left\{X_j\right\}$ represents the log-normal shadowing, and j refers to the j^{th} realization. $\delta(t)$ is the Dirac delta function. This channel model can be further simplified as

$$h(t)=\sum_{i=0}^{L_p-1}\gamma_i\delta(t-\tau_i) \tag{2.7}$$

where $L_p = K\times L$, $\gamma_i = X_j\alpha_{k,l}^{j}$, τ_i is the delay of the beam.

Hence, the received signal could be written as

$$r(t)=\sum_{i=0}^{L_p-1}\gamma_i s(t-\tau_i)+n(t) \tag{2.8}$$

Since the transmitted signal is encoded with a unique users' specified code, a template pulse sequence at the receiver is then correlated with the received signal. Ideally, the signal will be picked up at the intended user with the correct user's code, and suppressed otherwise. This also implies that the capacity of the system is related to the length of the users' code. A longer users' code accommodates more users. Many efforts have been devoted to the research on the impact of the users' codes on the system performance [6], [14], [31]-[35].

2.2.2 Pluses for Impulse Radio UWB

The shape of the pulse is very important to the UWB systems. Generally, it specifies the frequency spectrum of the transmitted signal. Well designed pulse shape ensures that maximum power is emitted from the transmitter within the FCC frequency mask. Thus better performance is expected at the receiver end. A variety of waveforms have been proposed for the IR system, including Gaussian, Rayleigh, Laplacian, and cubic monocycles [7].

Among them, the most frequently employed pulse shapes are derivatives of Gaussian function. The time domain expression of n^{th} order Gaussian derivative is [11]

$$p_n(t) = (-1)^{\lfloor (3n+1)/2 \rfloor} n!\pi^{-1/4} e^{-t^2/2\sigma^2} \sum_{k=0}^{\lfloor n/2 \rfloor} \frac{(-1)^k 2^{n+1/4-2k} \left(\frac{1}{2\sigma^2}\right)^{n/2+1/4-k} t^{n-2k}}{(n-2k)!k!\sqrt{(2n-1)!!}} , \qquad (2.9)$$

where $(2n-1)!! = (2n-1)\cdot(2n-3)\cdots 3\cdot 1$, σ is the standard deviation of the Gaussian function. This factor determines the power spectrum of the Gaussian monocycle and the pulse duration as well. Note that even order waveforms are even symmetric, and odd order waveforms are odd symmetric, as shown in Figure 2.1. The power spectrum densities of Gaussian monocycles from 1st to 5th order derivatives are depicted in Figure 2.2. All the monocycles are chosen such that they have the same pulse durations.

The FCC mask is mandatory, however too complex monocycle is not feasible from a circuits perspective of view. The optimization pulse design could be found in [7], [11], [12], [36]-[41]. In this thesis, a compromise choice is a 2nd order monocycle with its duration equal to 0.3 ns. The pulse is [7]

$$p_G(t) = A_G \left[1 - \left(\frac{t}{\sigma} - 3.5\right)^2\right] \exp\left[-0.5\left(\frac{t}{\sigma} - 3.5\right)^2\right] \quad , \qquad (2.10)$$

where A_G controls the amplitude, and pulse duration is $T_p = 7\sigma$.

The processing gain of an IR-UWB system could be approximated as [50], [51]

$$G \approx 10\log_{10}\frac{T_f}{T_p}dB \tag{2.11}$$

where T_f is the pulse repetition time. Usually the processing gain could be more than 10dB.

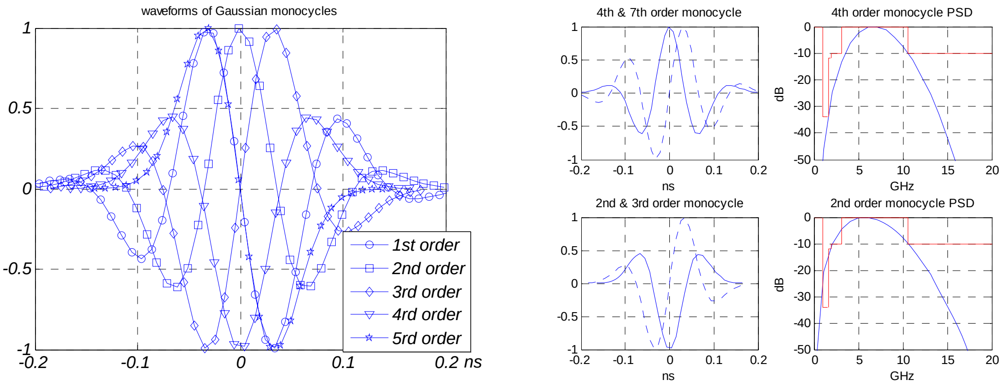

Figure 2.1 Waveforms of Gaussian Monocycles.

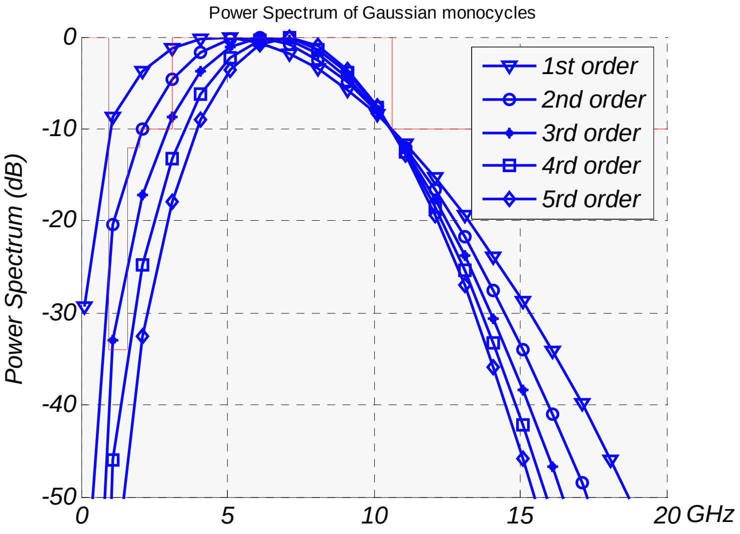

Figure 2.2 PSD of Gaussian monocycles.

2.2.3 Synchronization for Impulse Radio UWB Systems

An impulse radio (IR) UWB system transmits information via ultra-wideband pulses which have ultra-short pulse durations, usually less than a nanosecond. In the time domain perspective, the pulse is so short that to align it with the locally generated pulse is so critic. Even a slight misalignment between them may cause catastrophic performance degradation. Expected performance gain can be achieved only after precisely synchronized. Hence synchronization is one of the key points in the impulse radio UWB communication research.

At the beginning of the communication, there is little knowledge of the timing information at the receiver end. To establish reliable communication, synchronization should be achieved at both symbol level and frame level. A variety of synchronization schemes have been proposed in [4], [6], [8], [11]-[15], [19]-[24], [43].

A novel blind synchronization scheme called “Dirty Template” is proposed in [8] and [13]. By exploiting the rich multi-path diversity in the channel and noise contaminated received signal, the algorithm is able to obtain timing information without training data. To obtain frame level synchronization, the algorithm requires a high speed analog to digital converter (ADC) to get highly resolvable signal information. The speed may be up to multi-Giga hertz which leads to marvelous power consumption. This may be intolerable to some low power applications. However, the proposed scheme works quite well when targeting at symbol level synchronization which requires a reduced sampling rate.

An insight study of ML based synchronization scheme was reported in [4], [6], [13], [15], [19]-[24]. Both data aided and non-data aided ML timing acquisition were investigated [19]. With a set of sufficient observation data of the correlation receiver outputs, the proposed ML estimator gives the estimation of both channel fading parameter and the delay factor. This is an elegant way of synchronization and channel estimation as well. However, it takes too long to prepare the exhausting data pool. It is prohibitive to accumulate such large observation data pool in real life. Alternative way should be found.

There are also some multi-band (MB) UWB synchronization technologies being reported in the recent years [14], [52]-[54]. A pervasive study of a rapid acquisition scheme for MB-UWB system is proposed in [14]. The acquisition scheme exploits the inherent coded structure of the MB-UWB preamble, and was tested with two code candidates, namely the Barker code and CAZAC code. Although the acquisition scheme is developed for MB-UWB, it is also suitable for IR-UWB scenario.

The intrinsic rationale behind these synchronization schemes are all the same, that is by applying equation (1.2) and (1.3) (or some modified versions of these equations) the probability of synchronization is statistically maximized.

There is another detector categorized as constant false alarm rate detector (CFAR) [15], which gives an invariable false alarm rate regardless of the input noise level. One such detector structure is proposed by D. W. Trigg and A. G. Leach (1967) [16], called T&L detector structure [17] [18]. The detailed illustration will be referred later. Although it was not proposed for communication initially, some of its superior characters make it an ideal algorithm for IR-UWB synchronization.

Usually, the above synchronization schemes provide coarse acquisition of UWB systems. There is still error between the local pulse template and the received signal. Another fact is that, the channel is not a static one. Usually the received signal is a reflection of the EM wave to an object lying in the way between the two ends. To compensate this error and the drifting of the channel parameters, a delay lock loop (DLL) [2], [6], is employed to lock the local pulse generator with the received signal. The system block diagram is depicted in Figure 2.3. We shall see in a later chapter that the DLL (Figure 2.3) is a typical 2nd order close loop system, which is robust to various inputs. After the convergence of the tracking loop, fine synchronization is ultimately achieved, and the synchronization is robust to slow channel fading.

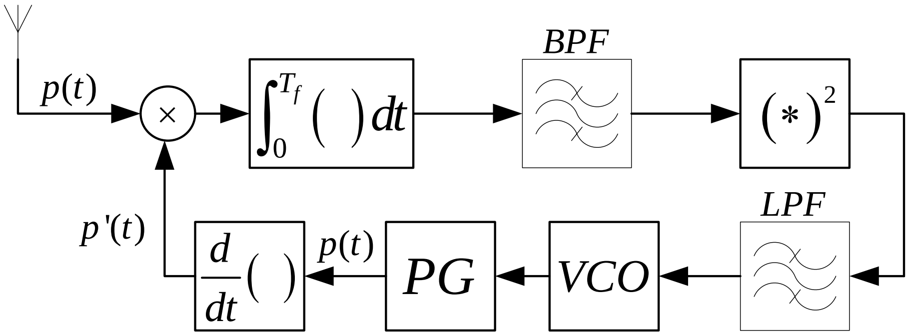

Figure 2.3 Block Diagram of a DLL.

The product of an n^{th} order Gaussian monocycle and a m^{th} order Gaussian monocycle is close to a $(m+n)^{th}$ order Gaussian monocycle [11], [12]. This character is very useful in predicting the behavior of a pulse location tracking loop. One important conclusion is drawn from Figure 2.3, the working curve of the close tracking loop is always an odd order Gaussian function which can be modeled as an odd symmetric function.

2.2.4 Receiver Structure

The receiver structure for IR-UWB systems is quite different from that of a

MB-UWB system. To effectively detect the transmitted information, receiver structure should be carefully conceived. Delicate but complex structures may give a better performance, however they also cost too much.

The optimum receiver of a communication system is the matched filter (MF) [2]. For BPSK systems, the bit error rate is

$$P_e = Q\left(\sqrt{SNR}\right). \tag{2.12}$$

This is also the performance upper-bound of the BPSK receiver.

The Transmitted Reference (TR) system was proposed in the 1920's for UWB communications, where the precise channel estimation is not possible [20]. In the recent years, researchers have developed a full set of theories for data detection of TR systems. A distinctive ML estimate of the TR based received signal was developed, and generalized likelihood ratio test (GLRT) was performed to determine the transmitted signal based on TR. The decision rule is simply [20]

$$\vec{r}_{TR}^{\,T}\vec{r}_d \underset{b=-1}{\overset{b=+1}{\gtrless}} 0 \tag{2.13}$$

where $\vec{r}_{TR}$ is the transmitted reference vector, and $\vec{r}_d$ is the received data vector to be determined combining with the TR. The TR system makes decisions based on all previous decisions. Thus by increasing the length of TR, performance improvement is expected. However the TR takes no information at all, increasing the TR length will reduce the information rate.

The most frequently investigated structure is called the RAKE receiver [21], [22], [23]. RAKE tries to collect as much signal energy as the received signal can provide. The relationship between RAKE finger number and the energy to be captured by

RAKE was reported by Dr. M. Z. Win and Dr. R. A. Scholtz [21]. Usually the number of dominant multi-path components is a large figure. As the number of fingers increasing, the energy captured increases as well. However, the improvement becomes negligible when the finger number exceeds 50. The total energy captured in a high SNR scenario is typically around 60%, and for a low SNR scenario, it is about 40%.

The optimum RAKE coefficients, $\tilde{\gamma}$, for a multi-path fading channel, with path fading coefficients γ, are chosen such that $\gamma = \tilde{\gamma}$ [2]. This is called the maximum ratio combining (MRC). The instantaneous SNR of the RAKE receiver is represented in equation (1.7). Thus the BER performance is [22]

$$p_e\left(\sqrt{\zeta_b}\right) = Q\left(\sqrt{\zeta_b}\right). \tag{2.14}$$

Usually the RAKE coefficients are chosen by applying the minimum mean square error criterion (MMSE). Thus, in practice, the RAKE coefficients are statistic values [23], and the expectation of $\tilde{\gamma}$, $E\{\tilde{\gamma}\} = \gamma$ [23].

2.3 Trigg and Leach Algorithm

The T&L algorithm was proposed first by D. W. Trigg and A. G. Leach in 1967 [16]. The T&L algorithm can effectively detect an abrupt change camouflaged in a noisy background [18]. It can also achieve constant false alarm rate (CFAR) detection. The false alarm probability is not a function of the background noise level. It is only related to the forgetting factor of the algorithm [17]. These two characters make it quite suitable for IR-UWB synchronization.

The impulse nature of the IR-UWB resembles the original working environment where T&L algorithm is applied. The initial purpose of the algorithm is to work as a fault detector where dominant noise presents and camouflages the fault pulses. For instance, in some control scenario, a fault occurs as a regularly appeared abrupt change. Usually such changes are naturally wide-band pulses.

The CFAR character enables the designer to suppress the false alarm rate by adjusting the forgetting factor. Generally, a smaller value of the forgetting factor results in a suppressed noise level at the detector output. Also by fixing the forgetting factor and the threshold value, which also means fixing the false alarm probability here, we can increase the detection probability by simply increasing the pulse power.

The proposed synchronization algorithm employs T&L detector to improve its performance. The performance analysis is also given in this thesis with closed form expressions. The whole receiver performance is also derived based on the synchronization performance. Thus, by the end of this thesis, a whole picture of the receiver is presented.

3 SYNCHRONIZATION FOR IMPULSE RADIO UWB SYSTEMS

Due to extremely short duty cycle of the UWB pulse, synchronization is the key of IR UWB communication systems. Any slight misalignment will result in failure of data communication. Conventional synchronization algorithms are mostly based on the matched filter (MF). In this chapter, a new synchronization algorithm is put forth. This algorithm is potentially better than conventional ones. The performance analysis and simulation verification will be addressed in later chapters.

3.1 Signal Modeling

For simplicity in both theoretical analysis and implementation, a 2nd order Gaussian monocycle is employed in this thesis. The adopted monocycle is given in (2.10) [7]

$$p(t) = A_G\left[1-(\frac{t}{\sigma}-3.5)^2\right]\exp\left[-0.5(\frac{t}{\sigma}-3.5)^2\right]. \tag{3.1}$$

The transmitted signal is modeled as a BPSK signal, which is a simplified version of (2.3)

$$s(t) = \sqrt{E_p}\sum_{n=-\infty}^{+\infty} a(n)\cdot c_{DS}\left(\lfloor n/N_f \rfloor\right) p\left(t-nT_f\right), \tag{3.2}$$

where the PN code sequence is a Barker code [14], $\{c_{DS}\} = \{1, 1, 1, -1\}$, such that the code’s auto-correlation function resembles a Dirac delta function, and the auto-correlation peak appears periodically. A single user scenario is considered. As long as synchronization is taken into account, the transmitted information sequence is also negligible. i.e. $\{a(n)\} = \{1\}$, thus

$$s(t) = \sqrt{E_p} \sum_{n=-\infty}^{+\infty} c_{DS} \left(\lfloor n/N_f \rfloor \right) p\left(t - nT_f \right). \tag{3.3}$$

To simplify the synchronization problem in a multi-path channel model specified in (2.6) and (2.7), instead of analyzing all paths, only the synchronization to the LOS path is considered. Hence the channel model for synchronization problem is further simplified as

$$h(t) = \gamma_0 \delta(t - \tau_0) , \tag{3.4}$$

where γ_0 and τ_0 stand for LOS path fading and propagation delay respectively. According to the channel model [10], γ_0 is a log-normal distributed RV with its distribution

$$20 \log_{10} \gamma_0 \sim N(\mu_0, \sigma_1^2 + \sigma_2^2) \tag{3.5}$$

where $\mu_0 = -\frac{\left(\sigma_1^2 + \sigma_2^2\right) \ln 10}{20}$, and $\sigma_1^2 = \sigma_2^2 = \left(\frac{4.8}{\sqrt{2}} \right)^2$. The received signal is then

$$r(t) = \gamma_0 s(t - \tau_0) + n(t) \tag{3.6}$$

where $n(t) \sim N(0, \sigma_w^2)$ is the AWGN.

3.2 Synchronizer Structure and Behavior Simulation

Basically, the receiver, after a low noise amplifier (LNA), starts with a sliding correlation receiver. The received signals are correlated with shifting template pulses. The proposed synchronization algorithm makes further processing to the correlator output and adjusts the delay of the local template pulse. Once the shifting template pulses are aligned with the received pulses, the synchronization is built up consequently. For this purpose, a complete solution to the synchronization problem is put forth which includes two parts: acquisition and tracking.

Acquisition is to determine the rough delay of the received pulse with respect to the local template. In acquisition, serially searching through all the potential delay is carried out, and the most likely delay is chosen. This position is regarded as a coarse timing delay from which a following step called tracking is initiated.

Tracking loop is to lock the template pulse delay to the received pulse, and maintain the alignment. Within the adjustable (but constrained) phase error, tracking loop is able to minimize the phase difference between the received pulses and the template automatically. In the following, the detailed algorithms will be discussed.

3.2.1 Acquisition Loop

The acquisition loop structure is depicted in Figure 3.1.

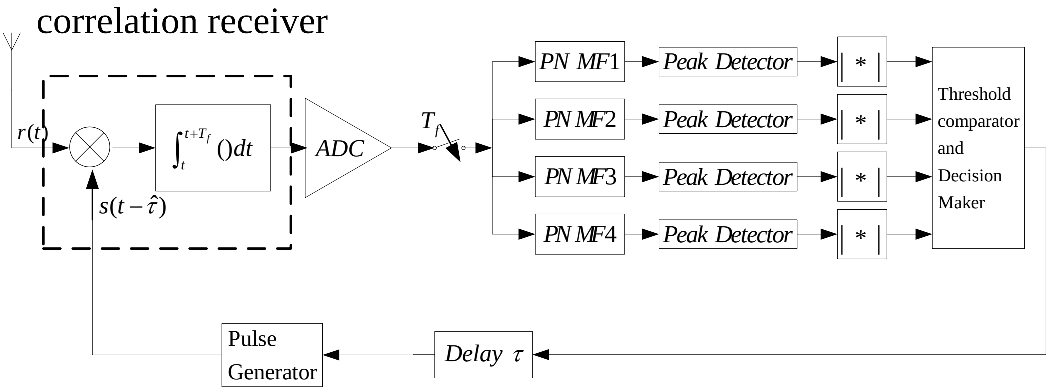

Figure 3.1 Acquisition Loop Structure.

It includes a correlation receiver, a sampler, four detector branches, a decision maker, a precision time delayer and a pulse generator. The sampler is sampling at the pulse repetition rate $1/T_f$. The sampled correlation value is matched to four shifted template Baker code in parallel. The maximum absolute value of the four detector outputs is selected, which is then compared with a threshold in the decision maker. If this maximum value is larger than the threshold, the corresponding Baker code template is regarded to have synchronized with the received pulse in phase. In this case, decision maker will stop the operation of time delayer and the close loop is locked. Otherwise, it is assumed no synchronization is set up. The time delayer then outputs a delayed clock signal which controls the pulse generator to produce a further delayed pulse. A typical working curve is depicted in Figure 3.2. As soon as one of the four branches gives a larger value than the threshold, the acquisition is accomplished.

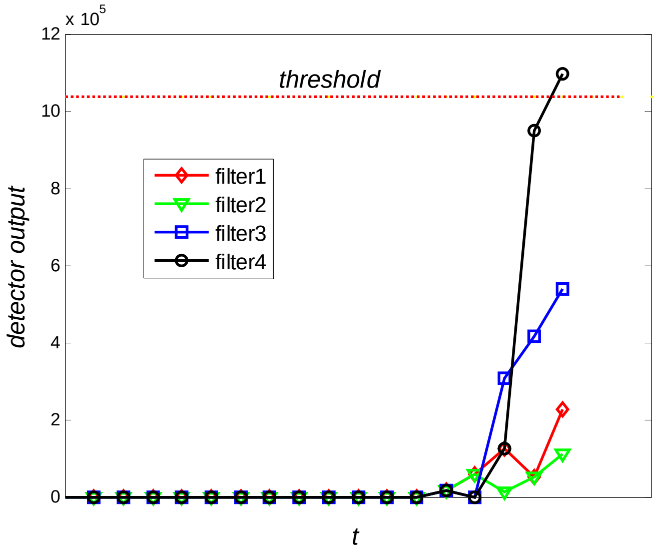

Figure 3.2 Typical Working Curves of the Proposed Acquisition Loop.

- PN code matched filter

The configuration of a PN code matched filter (MF) is shown in Figure 3.3. The conventional serially searching method for acquisition may cost a longer time to acquire timing information. Especially, when using a longer PN code, it may encounter a undesirable long searching time. To overcome this problem, a combination of serial timing searching and parallel phase matching is proposed, as shown in Figure 3.4. Four Baker code matched filters are operating in parallel during each iteration of the close loop (i.e. in per sampling interval). Since the Baker code only has four bits, thus four patterns are complete to encompass all possible shifted patterns of the Baker code. The outputs of the four MFs are

$$\begin{cases} \varepsilon_1(n) = x(nT_f) + x(nT_f - T_f) + x(nT_f - 2T_f) - x(nT_f - 3T_f) \\ \varepsilon_2(n) = x(nT_f) + x(nT_f - T_f) - x(nT_f - 2T_f) + x(nT_f - 3T_f) \\ \varepsilon_3(n) = x(nT_f) - x(nT_f - T_f) + x(nT_f - 2T_f) + x(nT_f - 3T_f) \\ \varepsilon_4(n) = -x(nT_f) + x(nT_f - T_f) + x(nT_f - 2T_f) + x(nT_f - 3T_f) \end{cases}, \qquad (3.7)$$

where $\varepsilon_i(n)$ is the MF output at the n^{th} sampling time.

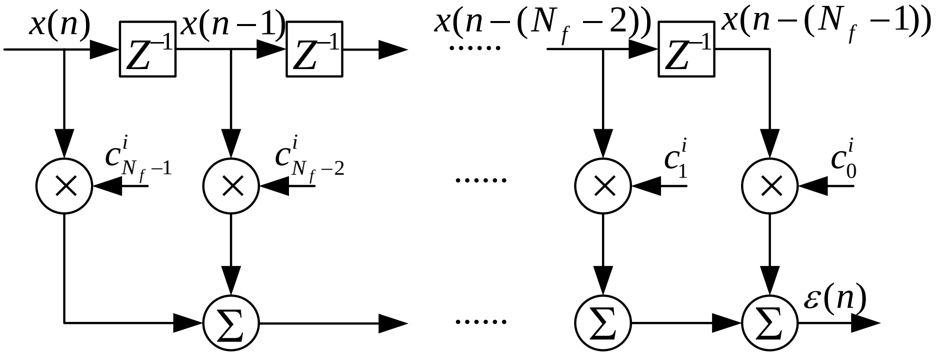

Figure 3.3 PN Code MF Structure.

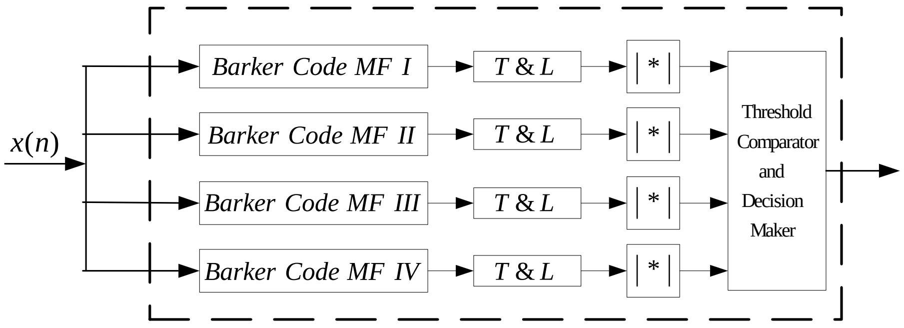

Figure 3.4 Parallel Search of Barker Code.

At each iteration, the received pulse sequence appears as a certain shifted Barker code pattern. When it is matched to one of the four matched filters patterns, ideally, that special branch gives a maximum value among those four. Obviously, longer PN code brings higher SNR at the MF output. However, there is a trade-off between the implementation cost and performance.

The MF outputs are consequentially fed into the T&L peak detectors.

- T&L peak detector

The peak detector is an implementation of T&L algorithm [16], [17]. The algorithm is rewritten in equations (3.8) through (3.10)

$$e_f(k) = (1-\rho)e_f(k-1) + \rho\varepsilon(k)\,, \tag{3.8}$$

$$e_a(k) = (1-\rho)e_a(k-1) + \rho\left|\varepsilon(k)\right|, \tag{3.9}$$

$$x_{fa}(k) = \frac{e_f(k)}{e_a(k)}\,. \tag{3.10}$$

where $\varepsilon(k)$ is the PN code MF output, ρ is a forgetting factor of a 1st order auto regressive moving average (ARMA) process, and ρ is supposed to be larger than but close to zero, typically $\rho \le 0.05$. $x_{fa}(k)$ is the T&L detector output. The whole detector structure is depicted graphically in Figure 3.5.

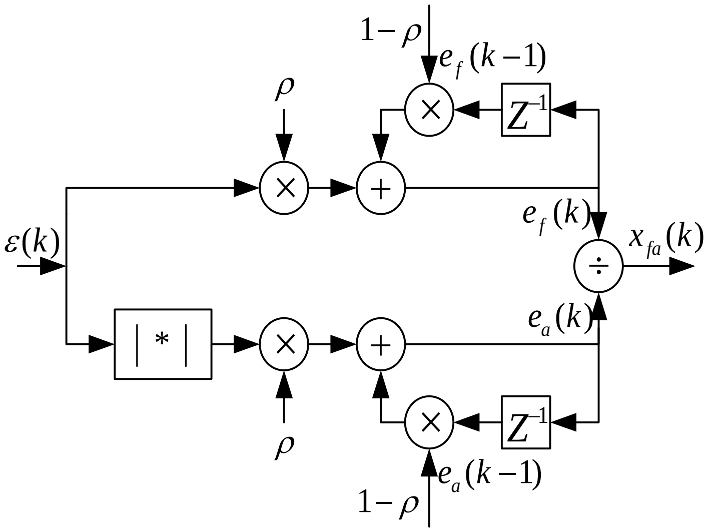

Figure 3.5 T&L Detector Structure.

A typical curve of the input versus the output is shown in Figure 3.6. The top figure is input signal of the detector at 0dB SNR. The bottom plot shows the output of the T&L peak detector. As shown in the Figure 3.6, although the input signal is camouflaged by the noise, the output of the T&L detector gives a conspicuous peak which distinguishes the noise contaminated peak from noise only signal. By setting a proper threshold value, the probability of correct detection is increased dramatically.

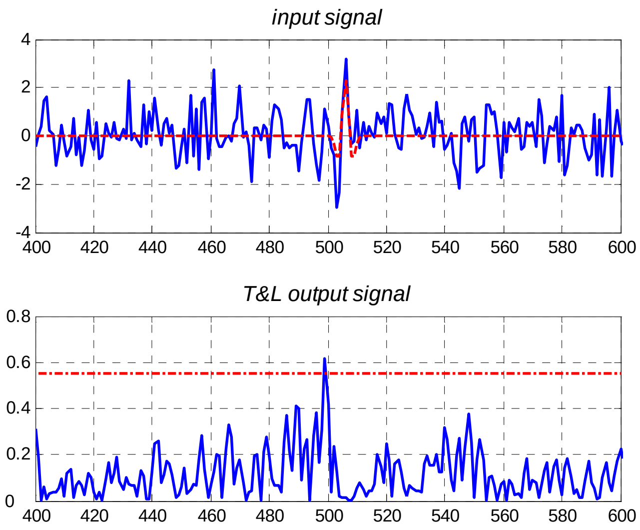

Figure 3.6 Typical Working Curve of the A T&L Peak Detector.

(3.8) and (3.9) are iterative expressions, and it is more convenient to express them in the summation form given by equations (3.11) and (3.12)

$$e_f(k) = \sum_{n=0}^{\infty} \rho(1-\rho)^n \varepsilon(k-n), \tag{3.11}$$

$$e_a(k) = \sum_{n=0}^{\infty} \rho(1-\rho)^n \left|\varepsilon(k-n)\right|. \tag{3.12}$$

The maximum absolute value of the four peak detector outputs is send into the decision maker and compared with a threshold. If the threshold is exceeded, an acquisition (ACQ) status is claimed and current delay value is fixed. Otherwise, another tiny step is imposed on the delayer, and the acquisition loop continues to search for the next possible phase.

Once the coarse acquisition is established, the synchronizer proceeds to the next stage, namely tracking, for more precise and robust synchronization.

3.2.2 Tracking Loop

As soon as the initial synchronization is established, the proposed synchronization scheme proceeds to the next stage. The tracking loop (TRK), see Figure 3.7, is triggered upon the completion of acquisition.

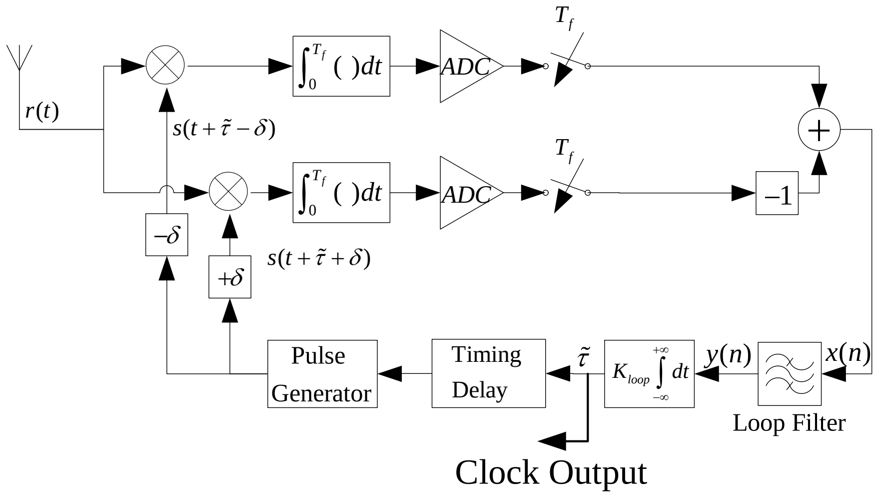

Figure 3.7 Tracking Loop Structure.

The tracking loop is essentially a digital Delay Lock Loop (DLL) which can track the slow fading of the transmission channel, including possible reflection, the Doppler drift, and the frequency drift of the transmitter and receiver oscillators [2], [6]. Tracking loop is able to minimize the delay difference between the received pulses and the local templates automatically. The sampler is sampling at the pulse repetition rate.

The difference between the leading branch and the lagging branch is then fed into the loop filter which is a typical low pass filter (LPF) to estimate the DC component of the differentiated input [6]. The loop will achieve its equilibrium point and be stabilized, when the outputs of the leading and lagging branch equal to each other.

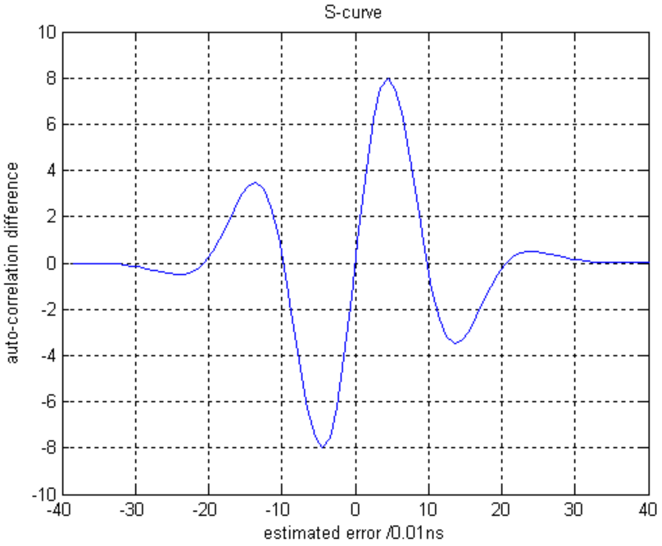

Figure 3.8 S-Curve of the DLL, with $\delta = 0.05ns$.

The DLL is actually a feedback servo system which locks to its optimum state subject to certain constrains. That is the input value of the loop filter should be within the linear operation interval of the S-curve which can be derived by subtracting the two correlation outputs of leading and lagging branches [6]. The characteristic of S-curve depends on the intrinsic property of the UWB impulse itself and the delay factor δ . Larger δ results in higher tolerance to acquisition error, and vise versa [6]. However, larger δ also indicates a slow convergence speed [6]. In this thesis, δ is chosen as $0.05ns$ which is a trade-off between the convergence speed and error tolerance. A typical S-curve is shown in Figure 3.8.

The difference between the leading and lagging branches, $x(n)$, is fed into the loop filter which in this thesis is chosen to be

$$y(n) = (1-\rho)\,y(n-1) + \rho x(n) \tag{3.13}$$

where typical value of the forgetting factor ρ is less than 0.05. The transfer function of the loop filter is

$$H(z) = \frac{\rho}{1-(1-\rho)\,z^{-1}}\,. \tag{3.14}$$

The magnitude response of the loop filter is depicted in Figure 3.9. The magnitude response depicts a low pass character. The damping to the DC component is 0dB, while other frequency components will all be suppressed.

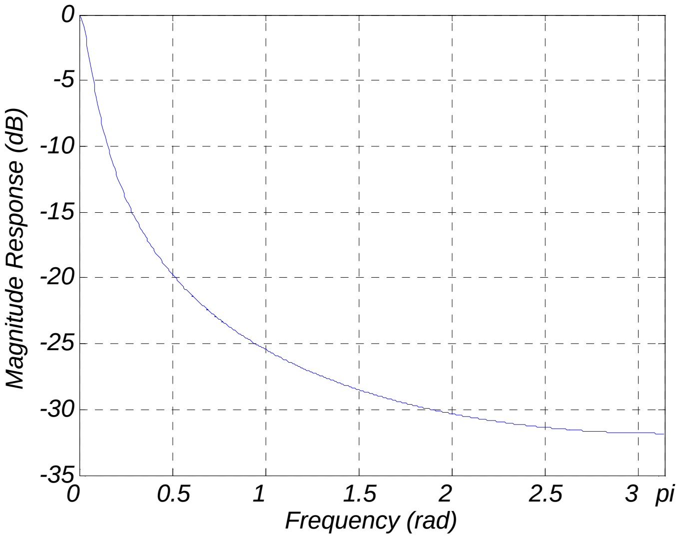

Figure 3.9 Magnitude Response of the Loop Filter.

The filter output is fed into an integrator which is also a low pass system from a signal processing perspective.

Next, the system transfer function of the closed-loop is analyzed. Assuming the impulse response of the loop filter as $f(t)$, integrator gain as g_c, multiplier gain as K_1, received signal power as P, the transfer function of the loop is, therefore [6]

$$H(s) = \frac{\hat{T}_d(s)}{T_d(s)} = \frac{K_d g_c F(s)}{s + K_d g_c F(s)} \tag{3.15}$$

where $K_d = K_1\sqrt{P/2} \times K_{slope}$, K_{slope} is the slope of the linear region on the S-curve, and $F(s)$ is the Laplace transform of the loop filter impulse response $f(t)$. As shown in [6], the response of the close loop system to a delta, step, ramps and parabolas inputs etc. can be pre-determined for various loop filter configurations. Such a tracking loop is a stable system [6].

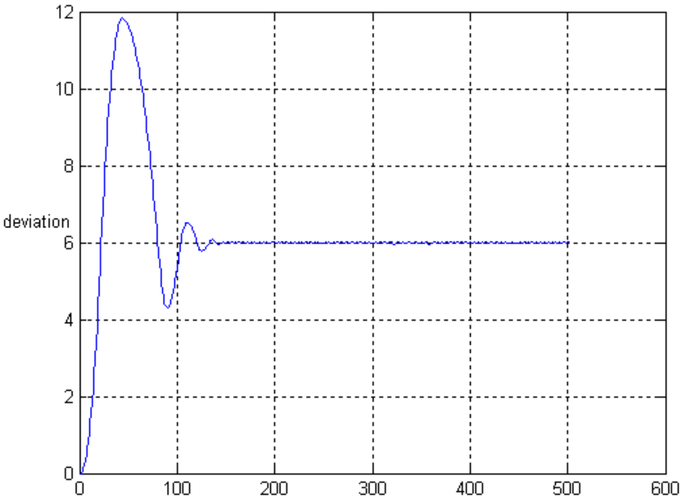

Figure 3.10 Typical Output of DLL.

A typical output of the DLL in the synchronization system is plotted in Figure 3.10. This is a typical step input response. The interpretation to this figure is that the stimulus of the DLL is the phase error between the received signal location and the local estimated location which is a DC component contaminated by the additive noise. The loop pass filter which in this case is modeled as a low pass filter which estimates the DC component contaminated by the noise. Since frequency components other than DC are all noise, they should all be suppressed by the loop filter. Figure 3.9 indicates that the loop filter works very well. However, there is certain amount of static error after the convergence of the system due to the residue noise [11] [12]. Such error is observed in Figure 3.11, in which a mismatch between the template and the received pulse is depicted.

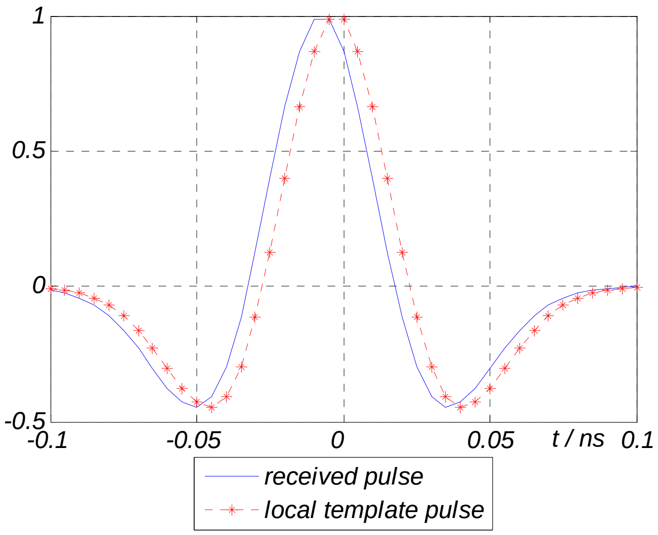

Figure 3.11 Pulse Position after Tracking.

The output of the integrator in Figure 3.7 drives the local generated pulse to a position according to the response curve of Figure 3.10. Different initial position may result in different response curves even if the DLL set-ups remain the same. However they are predictable with the knowledge of the transfer function (3.15)

Thorough analysis of UWB pulse tracking performance has been reported by Prof. R. A. Scholtz and et al [11], [12].

4 RAKE BASED IMPULSE RADIO (IR) UWB RECEIVER

To improve the performance of a RAKE receiver with the same input SNR, higher synchronization accuracy is required for each individual RAKE finger which guarantees high energy capture efficiency. A new RAKE receiver structure based on the proposed synchronization scheme is constructed in this chapter. We share see in the later chapters that better performance of this new structure is proved.

4.1 Signal Modeling

The transmitted signal is modeled as a simplified version of (3.2) where single user is assumed, i.e. $\{c_{DS}\} = \{\ 1\ \}$, and

$$s(t) = \sqrt{E_p} \sum_{n=-\infty}^{+\infty} a(n) \cdot p\left(t - nT_f\right), \tag{4.1}$$

where $p(t)$ is the monocycle employed in the IR UWB communication with unit energy, and E_p is the pulse energy. $\{a(n)\}$ is the data being transmitted and is modeled as a wide sense stationary (WSS) white Gaussian process.

The channel is modeled as a modified version of (2.7)

$$h(t) = \sum_{i=0}^{L_p - 1} \gamma_i \delta(t - \tau_i), \tag{4.2}$$

where L_p is the number of dominant paths, the multi-path fading coefficients $\{\gamma_i\}$ are assumed to be independent identical distributed (i.i.d.), and $\sum_{i=0}^{L_p-1} \gamma_i^2 = 1$ is assumed. $\{\gamma_i\}$ are most commonly modeled as log-normal distributed R.V.

Consequently, the received signal is

$$r(t)=\sum_{i=0}^{L_p-1}\gamma_i s(t-\tau_i)+n(t) \tag{4.3}$$

where $n(t)\sim N(0,\sigma_w^2)$ is the AWGN. Substituting (4.1) into (4.3) yields

$$r(t)=\sqrt{E_p}\sum_{n=-\infty}^{+\infty}a\left(n\right)\sum_{i=0}^{L_p-1}\gamma_i\cdot p\left(t-nT_f-\tau_i\right)+n(t)\,. \tag{4.4}$$

The interpretation to (4.4) is that for each bit $a(n)$, the pulse energy is randomly distributed among the L_p multi-paths' components. To simplify the analysis, the multi-path propagation delay $\left\{\tau_i\right\}$ are confined within a frame, i.e. $\tau_i<T_f$. To collect the energy and rebuild the severely distorted pulse, a RAKE receiver is usually employed.

4.2 Imperfectly Synchronized RAKE Receiver

4.2.1 Perfectly Synchronized RAKE

To collect as much energy as possible, ideally the receiver attempts to form a matched filter (MF) of the received signal [2]. Since the signal component in the received signal (4.4) is

$$u(t)=\sqrt{E_p}\sum_{i=0}^{L_p-1}\gamma_i\cdot p(t-\tau_i)\,. \tag{4.5}$$

The impulse response of the MF is [2]

$$\begin{aligned}h(t)&=u(T_f-t)\\&=\sqrt{E_p}\sum_{i=0}^{L_p-1}\gamma_i\cdot p\left(\left(T_f-t\right)-\tau_i\right).\end{aligned} \tag{4.6}$$

Consequently the receiver output at $t=nT_f$ is [2]

$$y(n)=\int_{(n-1)T_f}^{nT_f}r(\tau)h(t-\tau)d\tau\,. \tag{4.7}$$

This leads to the maximum output SNR [2]

$$SNR_0 = \frac{E_p}{\sigma_w^2}\int_0^{T_f} p^2(t)dt\,. \tag{4.8}$$

Decomposition of (4.6) gives an approach to form the MF for an IR UWB system.

$$\begin{aligned} h(t) &= \sqrt{E_p}\left(\gamma_0 \cdot p\left(\left(T_f - t\right) - \tau_0\right) + \gamma_1 \cdot p\left(\left(T_f - t\right) - \tau_1\right) + \cdots\right) \\ &= h_0(t) + h_1(t) + h_2(t) + \cdots\,. \end{aligned} \tag{4.9}$$

where $h_i(t) = \sqrt{E_p}\gamma_i \cdot p\left(\left(T_f - t\right) - \tau_i\right)$, is the impulse response of each individual matched filter. Accordingly the receiver output is

$$y(n) = \int_{(n-1)T_f}^{nT_f} r(\tau)h_0(t-\tau)d\tau + \int_{(n-1)T_f}^{nT_f} r(\tau)h_1(t-\tau)d\tau + \cdots\,. \tag{4.10}$$

Figure 4.1 specifies the receiver structure of (4.10), which is a typical RAKE receiver. With perfect knowledge of multi-path fading and delay, the RAKE receiver tends to be the optimum receiver as the finger number L_p tends to infinite.

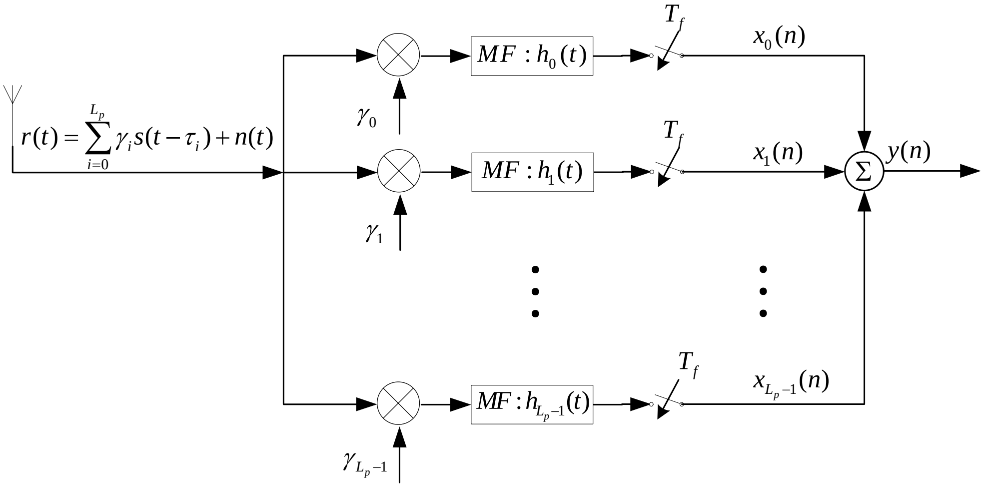

Figure 4.1 Receiver Structure of Equation (4.10).

However, the ideal MF is not realizable in real life. In a practical channel realization, the channel impulse response is comprised of infinite arrival rays. To capture all the energy beams, there should be infinite fingers, which is impractical. Another factor is that, the estimation of the channel fading and propagation delay can never be perfect. There is always certain amount of error. Thus the practical RAKE is usually a sub-optimum receiver.

Therefore the performance of a practical RAKE receiver will always subject to the accuracy of the channel parameter estimation, and finger numbers.

4.2.2 The RAKE Structure Based on Proposed the Synchronization Scheme

A practical RAKE receiver structure based on the proposed synchronization scheme is depicted in Figure 4.2. The received signal after a low noise amplifier (LNA) is fed into different branches of the RAKE. The propagation delay of each individual branch, τ_i, is first estimated with the proposed synchronization scheme. Once delay parameter is derived, the multi-path coefficients are then estimated. The synchronization is maintained by continuously tracking operation. Correct data decisions are given out when both channel parameter estimations are completed.

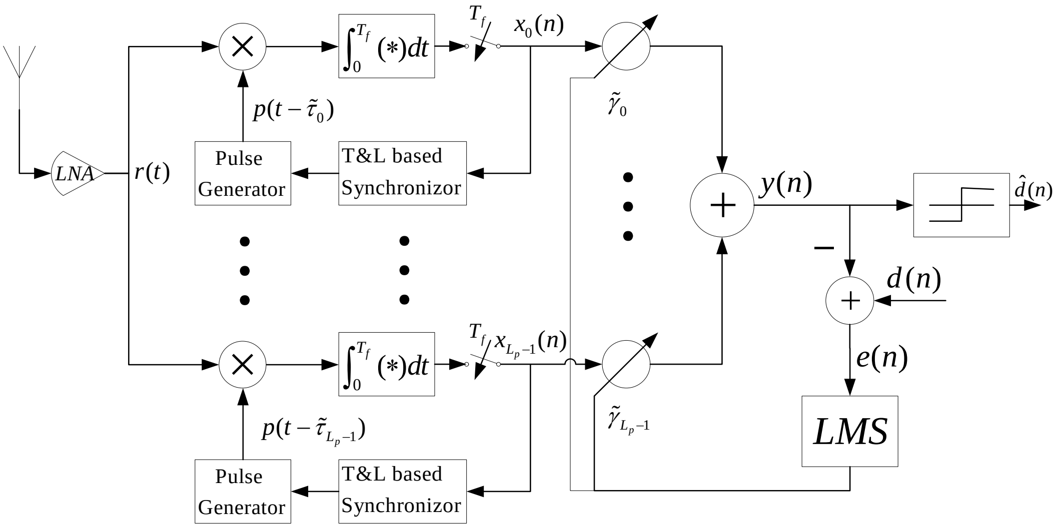

Figure 4.2 RAKE Structure Based on the Proposed Synchronization Scheme.

The synchronization process of each individual branch is elaborated in the previous chapter. However, a multi-branch parallel synchronization works slightly different. Since the sampling rate of the proposed receiver system is the pulse repetition rate, the receiver needs the number of ADCs as many as the number of the RAKE fingers. The starting point of each finger is different. The interleaving between two neighboring branches is chosen according to the mean arriving time of different cluster according to the channel model [10], such that the mean synchronization time of the total receiver is minimized. The acquisition of each branch is achieved at the detection probability $P(H_1 \mid H_1)\,(P_d(\zeta,\lambda))$ which is parameterized by the received SNR ζ and threshold value λ . Similarly, the false alarm rate $P(H_1 \mid H_0)$ that a branch captures a false peak is $P_{fa}(\lambda)$ which according to [17] is not affected by the SNR. Without loss of generality, assume that out of the L_p fingers, only L_c branches are correctly synchronized. And the remaining $L_e = L_p - L_c$ fingers are wrongly synchronized. Thus the estimation of the multi-path delay vector is

$$\tilde{\mathrm{T}}=\left[\underset{\left|\leftarrow\cdots L_c\cdots\rightarrow\right|}{\tilde{\tau}_0,\tilde{\tau}_1,\cdots,\tilde{\tau}_{L_c-1}},\underset{\left|\leftarrow\cdots L_e\cdots\rightarrow\right|}{\tilde{\tau}_{L_c},\cdots,\tilde{\tau}_{L_p-1}}\right]^T , \tag{4.11}$$

without loss of generality, first L_c elements are assumed correct.

To estimate the RAKE coefficients $\tilde{\Gamma} = \left[\tilde{\gamma}_1, \tilde{\gamma}_2, \cdots, \tilde{\gamma}_{L_p}\right]^T$, the minimum mean square error (MMSE) criterion is applied.

The output of the RAKE at the n^{th} frame is

$$y(n) = X^T(n)\tilde{\Gamma} \tag{4.12}$$

where $X(n) = \left[x_0(n), x_1(n), \cdots x_{L_{p-1}}(n)\right]^T$, and $x_i(n) = \int_{(n-1)T_f}^{nT_f} r(t)\,p(t-\tilde{\tau}_i)\,dt$ is the output of each branch after periodic sampling, $\tilde{\Gamma} = \left[\tilde{\gamma}_1, \tilde{\gamma}_2, \cdots, \tilde{\gamma}_{L_p}\right]^T$.

Different multi-path components are assumed statistically uncorrelated to each other, thus [24]

$$\frac{\int_0^{T_f} p(t-\tau_i)p(t-\tau_j)dt}{\int_0^{T_f} p^2(t)dt} = 0, \quad for\ i \neq j\,. \tag{4.13}$$

This equation indicates that cross-correlation between different pulse replica is zero. Since the vector $\tilde{\mathrm{T}}$ (from (4.11)) attempts to approach the true propagation delay vector T, it is reasonable to deduce that

$$\frac{\int_0^{T_f} p(t-\tau_i)p(t-\tilde{\tau}_j)dt}{\int_0^{T_f} p^2(t)dt} = 0, \quad for\ i \neq j \tag{4.14}$$

which means the correlation between the i^{th} pulse replica and the j^{th} local template pulse is zero.

To estimate Γ, MMSE criterion is applied, the cost function to be minimized is

$$\xi(n) = \left\| d(n) - y(n) \right\|^2, \tag{4.15}$$

where $d(n) = a(n)\int_0^{T_f} p_g^2(t)dt$ is the desired signal for BPSK systems and $a(n) = \pm 1$.

Substituting (4.12) into (4.15) yields

$$\xi(n) = a^2(n)\left[d^2(n) + \tilde{\Gamma}^T X(n)X^T(n)\tilde{\Gamma} - 2dX^T(n)\tilde{\Gamma}\right], \tag{4.16}$$

Take partial derivative of (4.16) with respect to $\tilde{\Gamma}$,

$$\frac{\partial \xi(n)}{\partial \tilde{\Gamma}} = 2\left[X(n)X^T(n)\right]\tilde{\Gamma} - 2\left[d(n)X(n)\right]. \tag{4.17}$$

Setting (4.17) equal to zero yields

$$\tilde{\Gamma} = \left[X(n)X^T(n)\right]^{-1}\left[X(n)d(n)\right]. \tag{4.18}$$

Equation (4.18) is the estimation of multi-path fading coefficients, by applying

MMSE criterion, based on the observed signal samples.

Equation (4.18) is also well known as the wiener solution [25] in which the matrix $X(n)X^T(n)$ is known as the correlation matrix of the input signal, and the vector $X(n)d(n)$ is known as the cross-correlation vector between input signal and desired signal.

Although wiener solution (equation (4.18)) gives an elegant answer to the MMSE estimation problem, direct applying equation (4.18) is refrained because of its expensive hardware cost. Especially the matrix inverse function is a formidable task in circuits or software design. It consumes too much power or system resource, and has limited application except for some military application.

An alternative way to bypass the matrix inverse problem is the famous least mean square (LMS) algorithm [25]. The iterative functions dramatically simplify the algorithm, and are listed in equations (4.19) through (4.21)

$$filtering: y(n) = X^T(n)\tilde{\Gamma}(n), \tag{4.19}$$

$$error: e(n) = d(n) - y(n), \tag{4.20}$$

$$updating\ taps: \tilde{\Gamma}(n+1) = \tilde{\Gamma}(n) + \mu e(n)X(n). \tag{4.21}$$

where μ is the iteration step which is a trade off between convergence speed and residue errors.

The mean square error (MSE) is monitored to see if convergence is achieved. The simulation is carried out at a typical setup with transmission rate at 100Mbps, SNR is 10dB, and a multi-path fading channel model [10] is employed with multi-path number equals to 5. A five fingers RAKE is employed for the simulation.

A typical MSE behavior is depicted in Figure 4.3. The behavior curve of MSE converged within only 20 frames. The convergence behavior of RAKE fingers also converged as soon as the MSE converged, as shown in Figure 4.4. The stable values of the tap-weights are trying to approach the multi-path fading coefficients that the fingers are in line with.

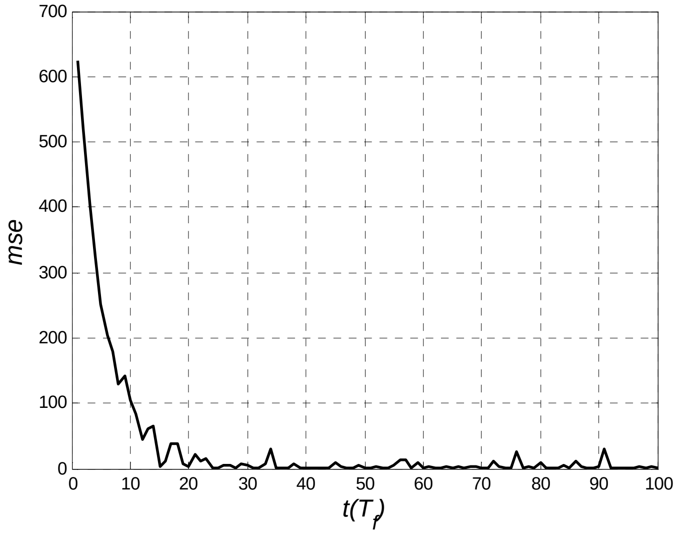

Figure 4.3 MSE Behavior of LMS Algorithm.

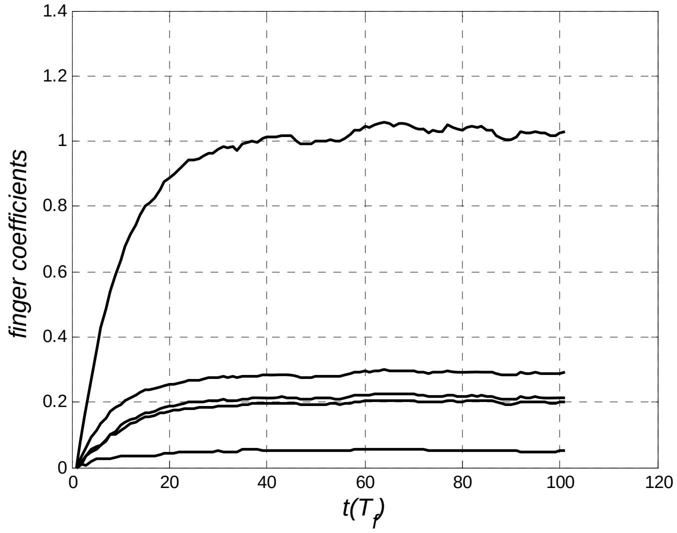

Figure 4.4 Convergence Behavior of RAKE Fingers.

5 PERFORMANCE ANALYSIS

In this chapter, the performance of a MF based and the proposed synchronization scheme are compared. After that, the performance of the RAKE receiver based on the proposed synchronization scheme is analyzed. In section 5.3, the computational complexity of the algorithm is compared with the so called Dirty Template scheme [13].

Through the analysis, 5dB to 10dB processing gain is verified by employing the proposed synchronization scheme. Therefore, better performance is expected for the corresponding RAKE receiver.

5.1 Correlation Receiver Performance

Usually, it is not feasible to construct the MF of the received signal. Simply because the channel involved in the transmission is a random realization which is not known at the receiver end. Thus a sub-optimum scheme, Figure 5.1, which neglects the channel effect, is often employed as a substitute. The receiver correlates the received signal with a local template, and is referred as a correlation receiver [2], [6], [15].

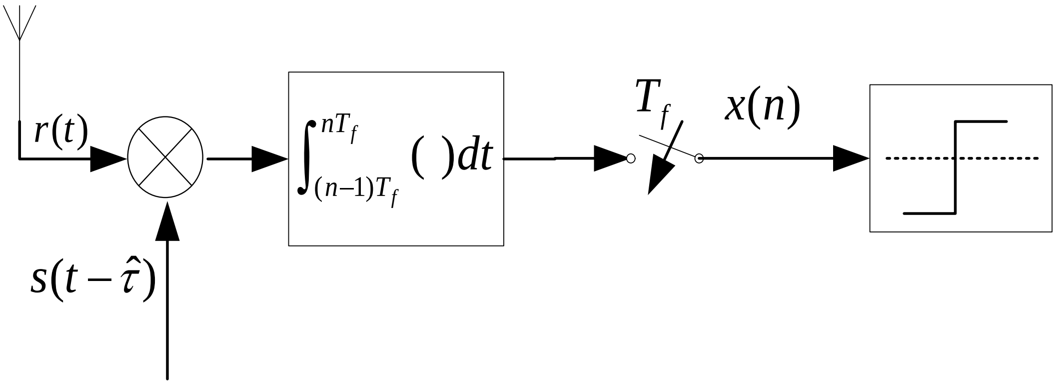

Figure 5.1 Typical Correlation Receiver.

AWGN channel is assumed. Therefore, the received signal is

$$r(t)=s(t-\tau)+n(t) \tag{5.1}$$

where $s(t)=\sqrt{E_p}\sum_{n=-\infty}^{+\infty}c(n)p(t-nT_f)$ is the transmitted signal, E_p is the pulse energy of the monocycle. $\{c(n)\}$ is a randomized code which is considered wide sense stationary (WSS). $n(t)$ is the AWGN with two sides power $\frac{N_0}{2}$. And the input SNR is defined as the SNR in the received signal equation (5.1).

The auto correlation function of the monocycle is approximately

$$\begin{aligned}R_p(\tau-\tilde{\tau})&=\int_0^{T_f}p(t-\tau)p(t-\tilde{\tau})dt\\&\approx E_p\delta(\tau-\tilde{\tau})\,.\end{aligned} \tag{5.2}$$

The sampled correlation output is

$$x(n)=\int_{(n-1)T_f}^{nT_f}r(t)s(t-\tilde{\tau})dt\,. \tag{5.3}$$

Substituting equation (5.1) into equation (5.3) yields

$$\begin{aligned}x(n)&=\int_{(n-1)T_f}^{nT_f}s(t-\tau)s(t-\tilde{\tau})dt+\int_{(n-1)T_f}^{nT_f}n(t)s(t-\tilde{\tau})dt\\&=\int_{(n-1)T_f}^{nT_f}c(n)p(t-nT_f-\tau)c(n)p(t-nT_f-\tilde{\tau})dt\\&\qquad+\int_{(n-1)T_f}^{nT_f}n(t)c(n)p(t-nT_f-\tilde{\tau})dt\\&=c^2(n)E_p\delta(\tau-\tilde{\tau})+c(n)\int_0^{T_f}n(t)p(t-\tilde{\tau})dt\,.\end{aligned} \tag{5.4}$$

Without loss of generality, $c(n)$ is assumed to unity. Thus

$$x(n) = E_p \delta(\tau - \tilde{\tau}) + w(t) \tag{5.5}$$

where $w(t) = \int_0^{T_f} n(t) p(t - \tilde{\tau}) dt$ is the additive noise after correlation, and its noise power is

$$E\left\{w(t)w(t')\right\} = E\left\{\int_0^{T_f} n(t) p(t - \tilde{\tau}) dt \int_0^{T_f} n(t') p(t' - \tilde{\tau}) dt'\right\},$$

therefore,

$$\begin{aligned} \sigma_w^2 &= \int_0^{T_f} E\left\{n^2(t)\right\} p^2(t - \tilde{\tau}) dt \\ &= \frac{N_0}{2} E_p . \end{aligned} \tag{5.6}$$

where E_p is the pulse energy, while $\frac{N_0}{2}$ is noise power. The output SNR is [27]

$$\zeta = \frac{E_p / T_p}{N_0 / 2} . \tag{5.7}$$

Compared with conventional carrier based communication system, where SNR is $\zeta_c = \frac{E_p / T_f}{N_0 / 2}$, same as the input SNR, with the same signal energy and information rate, the gain is

$$G = 10 \log_{10}\left(\frac{T_f}{T_p}\right) dB . \tag{5.8}$$

Synchronization for impulse radio system is essentially hypothesis detection problem. Two hypotheses are premised, namely pulse present and pulse absent, corresponding to the situations that synchronization is either achieved (H_1), or not (H_0). Thus equation (5.5) under either hypothesis is

$$\begin{cases} x(n)\big|_{H_0} = w(t) \\ x(n)\big|_{H_1} = E_p + w(t) \end{cases} . \tag{5.9}$$

The distribution of the received signal under either hypothesis is

$$\begin{cases} x(n)\,|_{H_0} \sim N\left(0,\sigma_w^2\right) \\ x(n)\,|_{H_1} \sim N\left(E_p,\sigma_w^2\right) \end{cases}. \tag{5.10}$$

To evaluate the detector performance, the receiver operation character (ROC) curve is introduced [15]. Two cases of events are concerned, namely successful detection $\left(H_1 \mid H_1\right)$ and false alarm $\left(H_1 \mid H_0\right)$. For a known threshold value λ, the false alarm probability is [15]

$$P_{fa}(\lambda) = Q\left(\frac{\lambda}{\sigma_w}\right), \tag{5.11}$$

and the detection probability is [15]

$$P_d(\lambda) = Q\left(\frac{\lambda - \sqrt{E_p}}{\sigma_w}\right) \tag{5.12}$$

and, finally, combine (5.11) and (5.12) yields

$$P_d\left(P_{fa}\right) = Q\left(Q^{-1}\left(P_{fa}\right) - \sqrt{\zeta}\right), \tag{5.13}$$

where ζ is the correlation output SNR equation (5.7). Equation (5.13) gives the ROC curve which is parameterized by the output SNR ζ. Figure 5.2 is the theoretic graph of equation (5.13). The duty cycle T_f / T_p is chosen as 25, thus the processing gain is, according to (5.8), approximately 14dB. The curves are marked by the output SNR ζ.

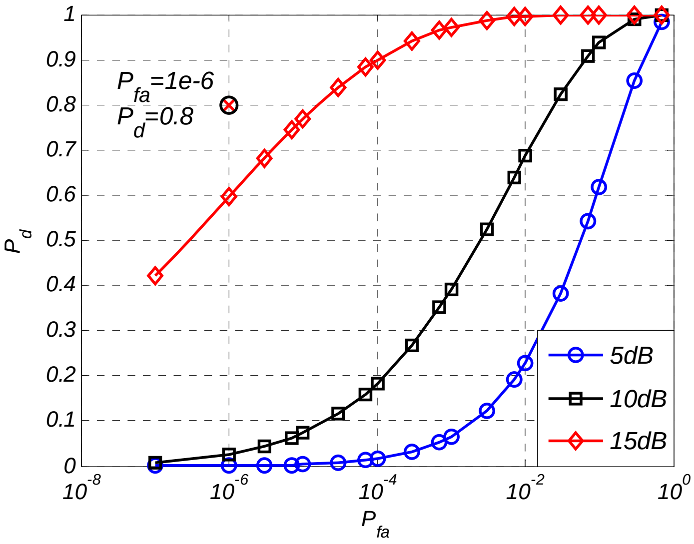

Figure 5.2 ROC Curve of a Correlation Receiver for IR UWB System.

A bench mark point is highlighted in Figure 5.2 at $P_{fa} = 10^{-6}$ and $P_d = 0.8$. Since the impulse only presents for a short period during a frame, the receiver is most frequently encountering noise only signal $x(n)|_{H_0}$, usually hundreds before meeting one correct point. Therefore, high detection probability and low false alarm rate are required.

Take the 15dB curve as an example, which lies beneath the bench-mark point in Figure 5.2, two alternatives are to be chosen for the receiver to work properly.

First choice is to simply increase the input SNR. This, according to Figure 5.2, works at the price of high power consumption. The increased pulse energy may exceed the FCC frequency mask as well.

Another choice is to employ some extra detector. Gain can be achieved at the price of computational complexity. However, it does not need to increase the signal power.

In previous chapters, a high performance detector called T&L detector is employed. Next we shall discuss the effects by employing T&L algorithm.

5.2 The Proposed T&L Based Synchronizer Performance Analysis

To improve the receiver performance, T&L detector is employed to modify the ROC curve. The receiver structure is shown in Figure 5.3.

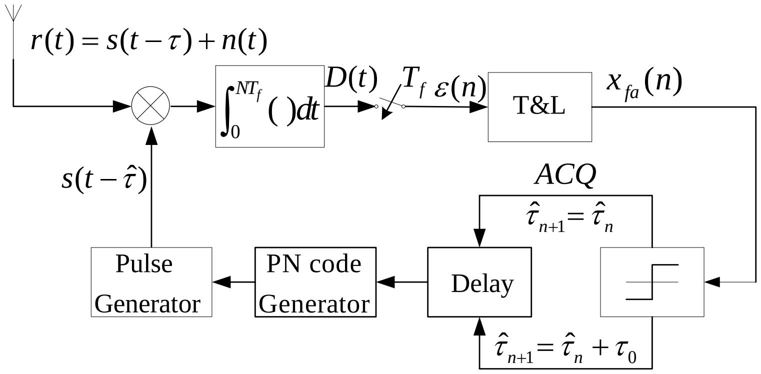

Figure 5.3 Simplified Synchronizer Structure.

The correlation receiver output signal under either hypothesis is listed in equations (5.9). The algorithm is rewritten as [16], [17], [18]

$$e_f(k)=\sum_{n=0}^{+\infty}\rho(1-\rho)^n\,\varepsilon(k-n) \tag{5.14}$$

$$e_a(k)=\sum_{n=0}^{+\infty}\rho(1-\rho)^n\,|\varepsilon(k-n)| \tag{5.15}$$

$$x_{fa}(k)=\frac{e_f(k)}{e_a(k)}. \tag{5.16}$$

where ρ is the forgetting factor, detailed analysis shows that the value of ρ is crucial to the performance of the proposed detector.

To close the performance analysis, the output PDF under both hypothetic inputs are needed.

The derivation of the PDF under H_0 is previously accomplished by Dr. Bengt Carlsson in his PhD dissertation, "*Digital Differentiating Filters and Model Based Fault Detection*" [17], 1989. It is well approximated by a Normal distributing function where the forgetting factor ρ is small enough, usually $\rho \le 0.05$. A graph of the output histogram under H_0 is plotted in Figure 5.4, in contrast with the Gaussian approximation given by equation (5.17). The simulation is carried out with $\rho = 0.05$, unit noise power and 100,000 samples being observed. The result shows that the Gaussian approximation is consistent with the observed T&L detector output distribution.

The asymptotical Gaussian distribution is [17]

$$x_{fa}\big|_{H_0} \sim N(0, \frac{\pi}{2}\frac{\rho}{2-\rho}) \tag{5.17}$$

This distribution shows a favorable character of the T&L detector: the false alarm rate will not be affected by the noise level in the received signal.

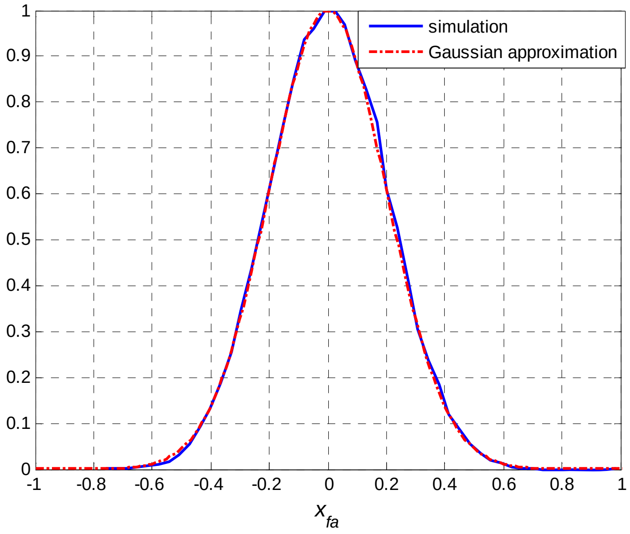

Figure 5.4 Distribution of T&L Detector Output under Hypothesis H_0.

The PDF under H_1 is not available which is also necessary to determine the T&L detector performance. To finally derive the PDF of x_{fa} under H_1, the task is divided into 3 steps.

1. determine the PDF of (5.14), $f_{e_f}(e_f)$;

2. determine the PDF of (5.15), $f_{e_a}(e_a)$;

3. determine the PDF of (5.16), $f_{X_{fa}}(x_{fa})$, based on the knowledge of $f_{e_f}(e_f)$ and $f_{e_a}(e_a)$.

5.2.1 Numerator Distribution

The numerator from equation (5.14) is $e_f(k) = \sum_{n=0}^{+\infty} \rho(1-\rho)^n \varepsilon(k-n)$. The input $\varepsilon(k)$ under H_1 is shown in equation (5.9). And the distribution of the input is

$$\varepsilon(k)|_{H_1} \sim N(\mu_\varepsilon, \sigma_w^2), \tag{5.18}$$

where $\mu_\varepsilon = E_p$. The linear combination of Gaussian R.V. is also Gaussian [28], thus e_f is also Gaussian, with its mean [28]

$$\begin{aligned}\mu_{e_f} &= E\left\{e_{fa}(k)\right\} \\ &= \sum_{n=0}^{\infty} \rho(1-\rho)^n E\left\{\varepsilon(k-n)\right\} \\ &= \mu_\varepsilon \big|_{n\to\infty},\end{aligned} \tag{5.19}$$

and the variance of e_f, $\sigma_{e_f}^2$ is [28]

$$\begin{aligned}\operatorname{var}\left\{e_f(k)\right\} &= \sum_{n=0}^{\infty} \rho^2(1-\rho)^{2n} \operatorname{var}\left\{\varepsilon(k-n)\right\} \\ &= \left.\frac{\rho}{2-\rho}\sigma_w^2\right|_{n\to\infty}.\end{aligned} \tag{5.20}$$

Hence, the distribution of e_f is

$$e_f\big|_{H_1} \sim N\left(\mu_\varepsilon, \frac{\rho}{2-\rho}\sigma_w^2\right). \tag{5.21}$$

To verify the validity of equation (5.21), simulation is carried out, and graphical result is depicted in Figure 5.5.

The graph shows that the simulation result is quite close to the Gaussian approximation. The simulation was carried out with a typical setup, unit noise power, $SNR = 10dB$, and $\rho = 0.05$, 50,000 samples were accumulated.

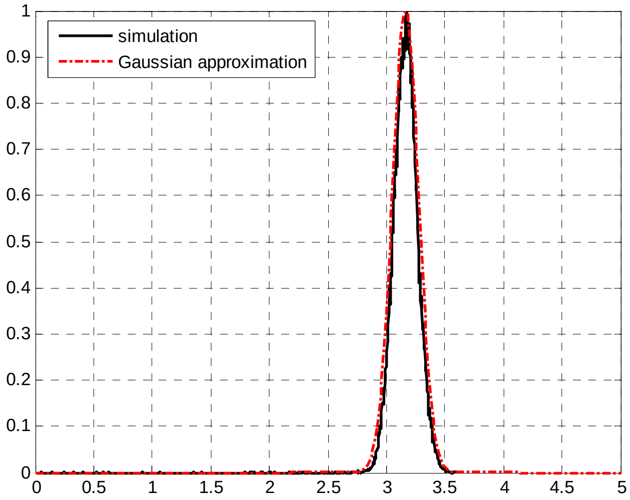

Figure 5.5 Numerator Distribution: Simulation vs. Gaussian Approximation.

5.2.2 Denominator Distribution

The denominator is $e_a(k) = \sum_{n=0}^{\infty} \rho(1-\rho)^n \left|\varepsilon(k-n)\right|$, expressed in equation (5.15). In stead of $\varepsilon(k)$, equivalently, its absolute value, $\left|\varepsilon(k)\right|$, could be treated as the input. Although the distribution of $\varepsilon(k)$ is Gaussian, its absolute value distribution is obviously non-Gaussian. However, the distribution could be derived analytically [28]

$$f_\Gamma(\tau(k)) = \frac{1}{\sqrt{2\pi\sigma_w^2}}\left[\exp\left(-\frac{(\tau(k)-\mu_\varepsilon)^2}{2\sigma_w^2}\right)+\exp\left(-\frac{(\tau(k)+\mu_\varepsilon)^2}{2\sigma_w^2}\right)\right], \quad (5.22)$$

where $\tau(k) = \left|\varepsilon(k)\right|$. Thus the mean of $\tau(k)$ is, according to its definition [28],

$$\mu_\tau = E\left\{\tau(k)\right\}$$

$$= \int_{-\infty}^{\infty} \tau\, f_\Gamma(\tau) d\tau$$

$$
\begin{aligned}
&= \frac{1}{\sqrt{2\pi\sigma_w^2}} \int_0^{\infty} \tau \exp\left(-\frac{(\tau-\mu_\varepsilon)^2}{2\sigma_w^2}\right) d\tau \\
&+ \frac{1}{\sqrt{2\pi\sigma_w^2}} \int_0^{\infty} \tau \exp\left(-\frac{(\tau+\mu_\varepsilon)^2}{2\sigma_w^2}\right) d\tau
\end{aligned}
$$

assign $x = \frac{\tau-\mu_\varepsilon}{\sigma_w}$, thus $d\tau = \sigma_w dx$, and $y = \frac{\tau+\mu_\varepsilon}{\sigma_w}$, $d\tau = \sigma_w dy$. Hence

$$
\begin{aligned}
\mu_\tau &= \frac{1}{\sqrt{2\pi\sigma_w^2}} \int_0^{\infty} (\sigma_w x + \mu_\varepsilon) \exp\left(-\frac{x^2}{2}\right) \sigma_w dx \\
&+ \frac{1}{\sqrt{2\pi\sigma_w^2}} \int_0^{\infty} (\sigma_w y - \mu_\varepsilon) \exp\left(-\frac{y^2}{2}\right) \sigma_w dy
\end{aligned}
$$

$$
\begin{aligned}
&= \frac{1}{\sqrt{2\pi}} \int_{-\frac{\mu_\varepsilon}{\sigma_w}}^{\infty} \sigma_w x \exp\left(-\frac{x^2}{2}\right) dx + \frac{1}{\sqrt{2\pi}} \int_{-\frac{\mu_\varepsilon}{\sigma_w}}^{\infty} \mu_\varepsilon \exp\left(-\frac{x^2}{2}\right) dx \\
&+ \frac{1}{\sqrt{2\pi}} \int_{\frac{\mu_\varepsilon}{\sigma_w}}^{\infty} \sigma_w y \exp\left(-\frac{y^2}{2}\right) dy - \frac{1}{\sqrt{2\pi}} \int_{\frac{\mu_\varepsilon}{\sigma_w}}^{\infty} \mu_\varepsilon \exp\left(-\frac{y^2}{2}\right) dy
\end{aligned}
$$

$$
\mu_\tau = \sqrt{\frac{2}{\pi}} \sigma_w \exp\left(-\frac{\mu_\varepsilon^2}{2\sigma_w^2}\right) + \left(1 - 2Q\left(\frac{\mu_\varepsilon}{\sigma_w}\right)\right) \mu_\varepsilon, \quad (5.23)
$$

where $Q(x) = \int_x^{\infty} \frac{1}{\sqrt{2\pi}} \exp\left(-\frac{1}{2} t^2\right) dt$, is the right-tail cumulative function. This result is verified by simulation with different signal power and noise power input

Similar to the procedure of $e_f(k)$, the mean of $e_a(k)$ is,

$$
\begin{aligned}
\mu_{e_a} &= E\{e_a(k)\} \\
&= \mu_\tau \qquad (5.24)
\end{aligned}
$$

To derive the variance of $e_a(k)$, the variance of $\tau(k)$ ($\tau(k) = |\varepsilon(k)|$) shall be derived first. The 2nd moment of $\tau(k)$ is, according to its original definition [28]

$$
\begin{aligned}
E\{\tau^2(k)\} &= \int_{-\infty}^{\infty} \tau^2 f_\Gamma(\tau) d\tau \\
&= \sigma_w^2 + \mu_\varepsilon^2, \qquad (5.25)
\end{aligned}
$$

and the variance of $\tau(k)$ is

$$\begin{aligned}\operatorname{var}\{\tau(k)\} &= E\{\tau^2(k)\} - E^2\{\tau(k)\} \\ &= \sigma_w^2 + \mu_\varepsilon^2 - \mu_\tau^2 . \qquad (5.26)\end{aligned}$$

Finally, the variance of $e_a(k)$, $\sigma_{e_a}^2$ is

$$\begin{aligned}\operatorname{var}\{e_a(k)\} &= \frac{\gamma}{2-\gamma}\operatorname{var}\{\tau(k)\}\Big|_{n\to\infty} \\ &= \frac{\rho}{2-\rho}(\sigma_w^2 + \mu_\varepsilon^2 - \mu_\tau^2) . \qquad (5.27)\end{aligned}$$

According to the central limited theorem, for large data observation, a R.V. distribution always tends to Gaussian. Thus, although a bit risky, the distribution of $e_a(k)$ was still modeled as Gaussian, and verified via simulation.

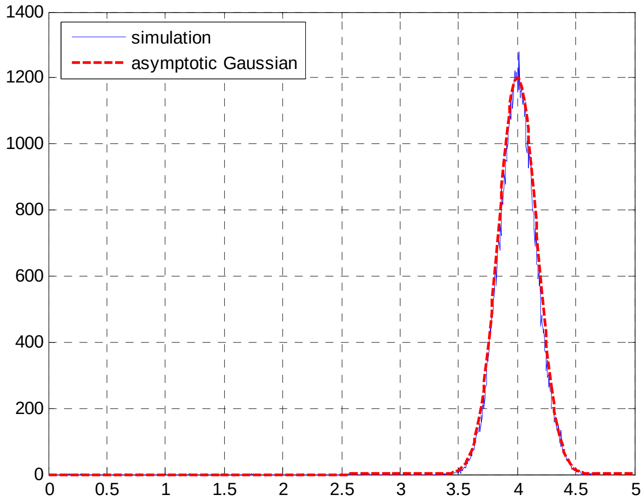

Figure 5.6 Denominator Distribution: Simulation against Gaussian Approximation.

The simulation result is depicted in Figure 5.6 in contrast with the asymptotic Gaussian approximation. The simulation was carried out with a typical setup, 50,000 samples were accumulated with unit noise power, $SNR = 10dB$, and $\rho = 0.05$. The solid line in the graph is the histogram of the simulation result. For large data accumulation, the observed distribution is close to the Gaussian asymptotic distribution. Thus the distribution of $e_a(k)$ is accurately approximated by

$$e_a\big|_{H_1} \sim N(\mu_{e_a}, \sigma_{e_a}^2) \tag{5.28}$$

5.2.3 Output Distribution

The distribution of numerator and denominator are

$$\begin{cases} e_f\big|_{H_1} \sim N(\mu_{e_f}, \sigma_{e_f}^2) \\ e_a\big|_{H_1} \sim N(\mu_{e_a}, \sigma_{e_a}^2) \end{cases}, \tag{5.29}$$

where the parameters are given in (5.19), (5.20), (5.24), and (5.27) respectively.

With the knowledge of both numerator and denominator distribution, we are now ready to derive the distribution of the quotient $x_{fa}(k) = \dfrac{e_f(k)}{e_a(k)}$.

By assuming independency between $e_f(k)$ and $e_a(k)$, the PDF of $x_{fa}(k)$ could be derived by completing the following integration [28]

$$\begin{aligned} f_{X_{fa}}(x_{fa}) &= \int_0^\infty e_a f_{e_f}(e_f) f_{e_a}(e_a) de_a \Big|_{e_f = e_a \cdot x_{fa}} \\ &= \int_0^\infty e_a f_{e_f}(e_a x_{fa}) f_{e_a}(e_a) de_a \,. \end{aligned}$$

Further working on this integration yields,

$$\begin{aligned} f_{X_{fa}}(x_{fa}) &= \frac{1}{2\pi\sigma_{e_f}\sigma_{e_a}} \int_0^\infty e_a \exp\left(-\frac{\left(e_a x_{fa} - \mu_{e_f}\right)^2}{2\sigma_{e_f}^2} \right) \exp\left(-\frac{\left(e_a - \mu_{e_a}\right)^2}{2\sigma_{e_a}^2} \right) de_a \\ &= \frac{\sigma_{e_f}^2 \sigma_{e_a}^2}{2\pi\sigma_{e_f}\sigma_{e_a}(\sigma_{e_a}^2 x_{fa}^2 + \sigma_{e_f}^2)} \cdot e^{-\frac{\sigma_{e_a}^2 \mu_{e_f}^2 + \sigma_{e_f}^2 \mu_{e_a}^2}{2\sigma_{e_f}^2 \sigma_{e_a}^2}} + B \cdot e^{\frac{\beta^2 - \alpha\lambda}{2\alpha\phi}} \cdot \sqrt{2\pi\phi/\alpha} \cdot Q(-\frac{\beta}{\sqrt{\alpha\phi}}) \end{aligned}$$

$$= \frac{\sqrt{\phi}}{2\pi\alpha} \cdot e^{-\frac{\lambda}{2\phi}} + \frac{\beta}{2\pi\alpha} \cdot e^{\frac{\beta^2-\alpha\lambda}{2\alpha\phi}} \cdot \sqrt{\frac{2\pi}{\alpha}} \cdot Q\left(-\frac{\beta}{\sqrt{\alpha\phi}} \right). \quad (5.30)$$

where $Q(x) = \int_x^{\infty} \frac{1}{\sqrt{2\pi}} \exp\left(-\frac{1}{2} t^2 \right) dt$, $\alpha = \sigma_{e_a}^2 x_{fa}^2 + \sigma_{e_f}^2$, $\beta = \sigma_{e_a}^2 \mu_{e_f} x_{fa} + \sigma_{e_f}^2 \mu_{e_a}$, $\lambda = \sigma_{e_a}^2 \mu_{e_f}^2 + \sigma_{e_f}^2 \mu_{e_a}^2$, $\phi = \sigma_{e_a}^2 \sigma_{e_f}^2$. And the parameters are listed in (5.19), (5.20), (5.24), and (5.27), i.e. $\mu_{e_f} = \mu_\varepsilon$, $\mu_{e_a} = \sqrt{\frac{2}{\pi}} \sigma_w \exp\left(-\frac{\mu_\varepsilon^2}{2\sigma_w^2} \right) + \left(1 - 2Q\left(\frac{\mu_\varepsilon}{\sigma_w} \right) \right) \mu_\varepsilon$, $\mu_\tau = \mu_{e_a}$, $\sigma_{e_a}^2 = \frac{\rho}{2-\rho} (\sigma_w^2 + \mu_\varepsilon^2 - \mu_\tau^2)$, and $\sigma_{e_f}^2 = \frac{\rho}{2-\rho} \sigma_w^2$. It is not difficult to find out that all the parameters are finally related to signal level μ_ε and noise level σ_w^2. Thus it is parameterized by the correlation output SNR ζ_0. However, the equation (5.30) is too complicated to use. By employing the asymptotic cumulative function $Q(x) \approx \frac{1}{\sqrt{2\pi} x} \exp(-\frac{1}{2} x^2)$, equation (5.30) could be simplified as

$$f_{X_{fa}}(x_{fa}) = \frac{\sqrt{\phi}}{2\pi\alpha} \cdot e^{-\frac{\lambda}{2\phi}} + \frac{\beta}{2\pi\alpha} \cdot e^{\frac{\beta^2-\alpha\lambda}{2\alpha\phi}} \cdot \sqrt{\frac{2\pi}{\alpha}} \cdot \left(1 - Q\left(\frac{\beta}{\sqrt{\alpha\phi}} \right) \right)$$

$$= \frac{\beta}{\alpha\sqrt{2\pi\alpha}} \cdot e^{\frac{\beta^2}{2\alpha\phi}} \cdot e^{-\frac{\lambda}{2\phi}}. \quad (5.31)$$

The validity of (5.31) is verified by numerical results plotted in Figure 5.7.

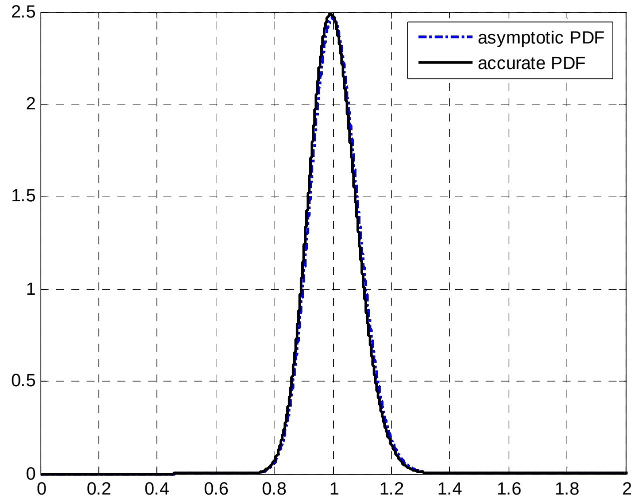

Figure 5.7 PDF of T&L Detector output under H_1.

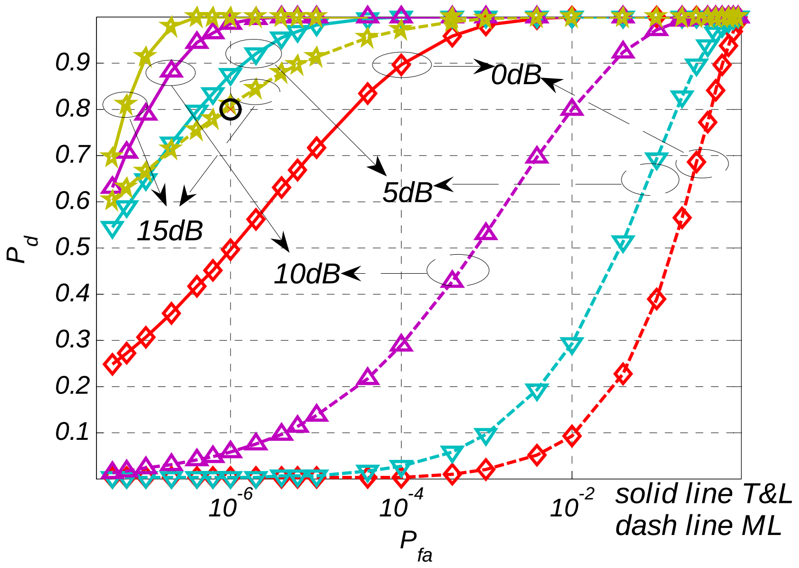

Figure 5.8 T&L Detector Performance with ***ρ=0.04.***

To derive the ROC of the detector, we first derive the false alarm probability from equation (5.17),

$$P_{fa}(\lambda) = Q\left(\lambda \Big/ \sqrt{\frac{\pi}{2}\frac{\rho}{2-\rho}}\right) \tag{5.32}$$

and the detection probability from equation (5.30)

$$P_d(\zeta,\lambda) = \int_{\lambda}^{+\infty} f_{X_{fa}}(x_{fa})dx_{fa} \tag{5.33}$$

where λ is the threshold value and ζ is the input SNR.

The performance of the T&L detector is not easily derived in a closed form. However, numerical results could be derived and depicted in Figure 5.8 with $\rho = 0.04$. The comparison of the ML based detector and T&L detector shows that large gain can be achieved by employing a T&L detector. For instance, to work above the bench mark point, a conventional ML based detector needs an correlation output SNR of at lease 15dB, however, by employing a T&L detector, only 5dB output SNR is required to achieved the bench mark point.

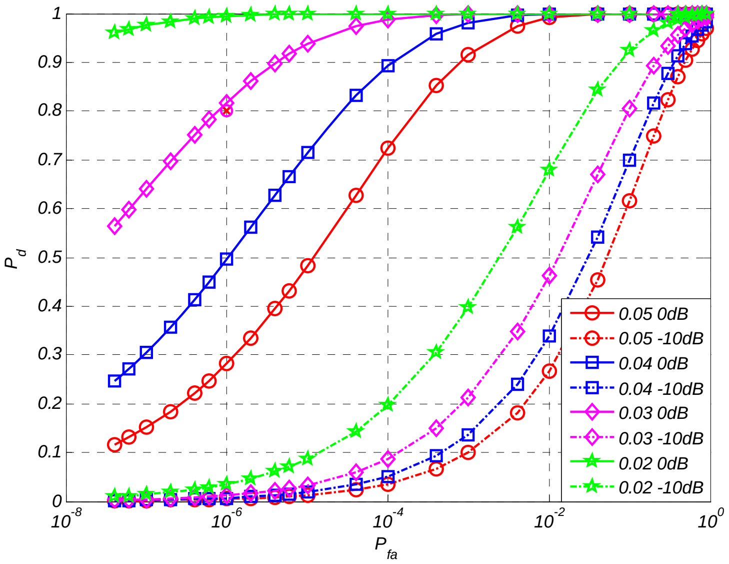

Figure 5.9 Effect of Forgetting Factor $\boldsymbol{\rho}$ on the ROC.

Figure 5.9 shows the ROC curve of a T&L based detector with varying forgetting factor ρ. Two sets of numerical results are depicted with correlation output SNR at -10dB and 0dB respectively. The graph shows another favorable character of the proposed detector. Unlike ML based receiver, the ROC of a T&L detector can be modified without change of SNR input. This indicates that receiver works differently with varying forgetting factor ρ. For instance, with the same correlation output SNR of 0dB, for the values $\rho = 0.05$ and $\rho = 0.04$, the corresponding ROC works below the bench mark point. While for the values $\rho = 0.03$ and $\rho = 0.02$, the ROC works above the bench mark point. The conclusion is that smaller ρ brings better performance. However, slower convergence speed also comes along with a smaller ρ value. It is a trade-off between ROC performance and convergence performance.

5.2.4 Proposed Synchronization Scheme Performance

The proposed detector depicted in Figure 5.3, is a concatenation of a correlation receiver and a T&L peak detector. Thus, the whole detector performance is also a concatenation of these two. From the SNR perspective, the correlation receiver provides a gain which is specified by $G = 10\log_{10}\left(\frac{T_f}{T_p}\right)dB$ (5.8). Consequently, the effect of the correlation receiver could be simply replaced by increasing the SNR by a factor which is specified in (5.8).

Finally, the detector performance is concluded with slightly modified equations (5.32) and (5.33) by imposing the UWB gain introduced by the correlation receiver. Although the closed-form ROC curve is difficult to obtain, the numerical results are still tractable. The graphic depictions of these numeric results with different choices of the forgetting factor ρ value were shown in Figures 5.10~5.11.

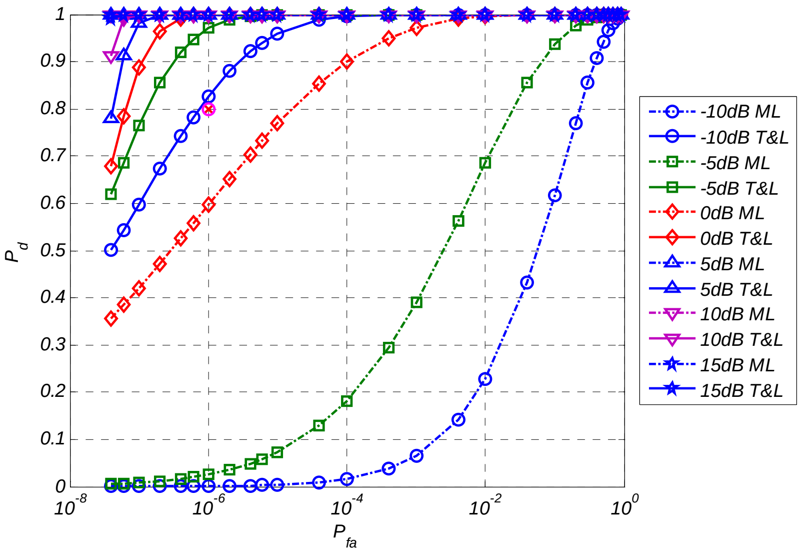

Figure 5.10 ROC of the Proposed Detector against ML Detector with ***ρ=0.04***.

A set of performance comparisons between conventional UWB correlation receiver (Figure 5.2) and proposed T&L based UWB signal detector is depicted in Figure 5.10 with different correlation input SNR values and $\rho = 0.04$. The conclusion is that T&L detector brings tremendous gain. For example, to work above the bench mark point, conventional receiver requires 5dB correlation input SNR. However, input SNR of -10dB is sufficient to support the T&L based detector to work at the same region.

Numerical results have also been derived to find out the effect of Forgetting Factor ρ on the total receiver ROC. Figure 5.11 shows the results graphically. Again the bench mark point is placed to give a reference to compare the performance. It can be seem in the Figure 5.11 that with decreasing forgetting factor values at the input SNR, the performance is improving. The conclusion is simply smaller ρ indicates better performance. However, smaller ρ indicates slower convergence speed.

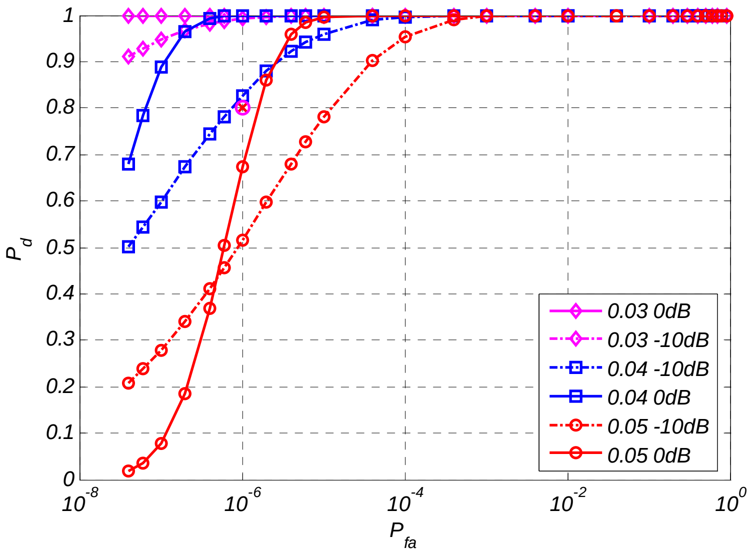

Figure 5.11 Effect of Forgetting Factor $\boldsymbol{\rho}$ on the total ROC.

5.2.5 Further Discussion of Proposed Synchronization Scheme with Log-normal Channel Fading

Previously, all the discussions are based on the AWGN channel model. However, a more practical situation is that the transmitted signal travels through a multi-path channel, as equation (2.6). Due to the high resolvability of the UWB system, no inter path overlapping is considered [11]. Therefore, for the synchronization of each RAKE finger, the channel model could be simplified as

$$h(t) = \gamma_0 \delta(t - \tau_0) \tag{5.34}$$

where $20\log_{10}\gamma_0 \sim N(\mu_0, \sigma_1^2 + \sigma_2^2)$ with $\mu_0 = -\frac{\left(\sigma_1^2 + \sigma_2^2\right)\ln 10}{20}$, $\sigma_1^2 = \sigma_2^2 = \left(\frac{4.8}{\sqrt{2}}\right)^2$, and $\tau_0 \sim U(0, T_f)$, which is a uniform distribution. Hence the received signal is

$$r(t) = \gamma_0 s(t - \tau_0) + n(t) \tag{5.35}$$

where $n(t)$ is AWGN with two sides power spectrum $\frac{N_0}{2}$. Thus the output of the correlation receiver becomes

$$\begin{cases} \varepsilon(n)\big|_{H_0} = w(t) \\ \varepsilon(n)\big|_{H_1} = \gamma_0 E_p + w(t) \end{cases} \tag{5.36}$$

for a fixed channel realization, where $w(t) \sim N(0, \sigma_w^2)$ is the additive noise after correlation receiver, with $\sigma_w^2 = \frac{N_0}{2} E_p$.

It is conceivable that the detector performance will be different if channel effect is imposed. The major impact is that instead of equation (5.18) the signal under H_1 becomes

$$\varepsilon(k)\,|_{H_1} \sim N(\mu_\varepsilon, \sigma_w^2) \tag{5.37}$$

where the signal component $\mu_\varepsilon = \gamma_0 E_p$.

With a fixed multi-path fading coefficient, all the other analysis remains the same. Thus the PDF of output signal under H_1, $f_{X_{fa}|H_1}\left(x_{fa}\right)$ is the same as equation (5.30) with μ_ε parameterized by lognormal fading R.V. γ_0. Thus

$$f_{X_{fa}|H_1}\left(x_{fa}\right) = \int_{-\infty}^{+\infty} f_{X_{fa}|H_1}\left(x_{fa}, \gamma_0\right) f_{\Gamma_0}(\gamma_0) d\gamma_0 \,. \tag{5.38}$$

where $f_{\Gamma_0}(\gamma_0)$ is the distribution of the lognormal channel fading coefficient. Equation (5.38) is parameterized by the input SNR ζ_0. However, the detector output distribution under H_0 is not affected by the multi-path fading and remains

$$x_{fa}\,|_{H_0} \sim N(0, \frac{\pi}{2} \frac{\rho}{2-\rho}) \,. \tag{5.39}$$

Equations (5.38) and (5.39) finally conclude the performance analysis of the proposed T&L based synchronization algorithm when suffering from multi-path fading. This result is particularly useful when evaluating the performance of an imperfectly synchronized RAKE receiver for UWB IR communication systems. For each individual RAKE finger, it could be well modeled as the situation discussed in this section.

5.3 Algorithm Computational Complexity Analysis

The computational complexity issue is critical for the hardware implementation of the algorithm, especially for portable devices. In this section, the computational complexity of the proposed algorithm is analyzed and compared with another candidate, the Dirty Template scheme.

The timing uncertainty for both algorithms were assumed uniformly distributed over the interval $\left[0,T_f\right]$, and homogenous searching steps were adopted. The searching steps were the same for both schemes. To compare the two algorithm equally, identical detection performance were presumed, i.e. same P_d and P_{fa}. With the above assumption, the acquisition times for both schemes are statistically the same. Hence the complexity analysis is to compare the computational burden of each searching step.

The Dirty Template scheme is essentially an implementation of Matched Filter (MF). To match the impulse response of a UWB monocycle over a channel, the bandwidth should be at least twice the bandwidth of the UWB monocycle which is more than 20GHz. Assume a 100Mbps sequence is transmitted, the shortest Dirty Template length is T_f, which is a more than 200 taps FIR filter. For each searching step, a total of 200 multiplications and 200 additions are performed. In hardware implementation, a better solution for the multiplication is a look-up table since the digital multipliers is prohibited.

The computational complexity of the T&L based synchronization scheme is then analyzed. For each step, the equation (3.8) requires 2 multiplications and 1 addition. Equation (3.9) requires 2 multiplications, 1 addition, and one comparison to obtain the absolute value of the incoming sample. Equation (3.10) requires a division. In hardware implementation, the product of a register and a forgetting factor could be substitute with a register shifting operation. In this case, the equations (3.8) requires 2 register shifting operations and 2 additions. And so does the equation (3.9). The division operation could also be mapped to a look-up table. The comparison results are summarized in the following table.

	Additions	Multiplications	Look-up Table	Division	Register Shifting
Dirty Template	200	200	1	0	0
T&L based	2	4	1	1	4

Direct comparison reveals an intuitive conclusion that the proposed T&L based synchronization scheme is relatively more efficient.

5.4 RAKE Performance

The proposed RAKE receiver structure is depicted in Figure 4.2 and the algorithm is elaborated in section 4.2.2. The received signal is equation (4.5) for a multi-path channel model specified in equation (4.2) which is

$$h(t) = \sum_{i=0}^{L_p-1} \gamma_i \delta(t-\tau_i)\,, \tag{5.40}$$

with the assumption that the i.i.d. R.V.s γ_i are to fulfill $\sum_{i=0}^{L_p-1} \gamma_i^2 = 1$.

The received signal for the n^{th} symbol is

$$r(t) = a_n \sum_{i=0}^{L_p-1} \gamma_i p_g(t-\tau_i) + n(t)$$

$$= a_n \Gamma^T P_G(\tau) + n(t) \qquad (5.41)$$

where $\Gamma = \left[\gamma_1, \gamma_2, \cdots, \gamma_{L_p}\right]^T$ and $P_G(\tau) = \left[p_g(t-\tau_1), p_g(t-\tau_2), \cdots, p_g(t-\tau_{L_p})\right]^T$. Thus the output of the correlation receivers is

$$X(n) = \int_{(n-1)T_f}^{nT_f} r(t) P_G(\tilde{\tau}) dt. \qquad (5.42)$$

Consequently, the RAKE receiver output is

$$y(n) = X^T(n)\tilde{\Gamma},$$

and represented as

$$y(n) = a_n \sum_{i=0}^{L_p-1} \gamma_i \tilde{\gamma}_i \int_0^{T_f} p_g(t-\tau_i) p_g(t-\tilde{\tau}_i) dt + \sum_{i=0}^{L_p-1} \tilde{\gamma}_i \int_0^{T_f} n(t) p_g(t-\tilde{\tau}_i) dt. \qquad (5.43)$$

The RAKE coefficients $\tilde{\Gamma} = \left[\tilde{\gamma}_1, \tilde{\gamma}_2, \cdots, \tilde{\gamma}_{L_p}\right]^T$ are estimated by equation (4.18), where the desired signal $d(n) = \sum_{n=-\infty}^{+\infty} a_n p_g(t - nT_f)$ is the replica of transmitted signal. To evaluate the whole structure performance, the distribution of the RAKE coefficients should be determined first.

The first term in equation (4.18) is

$$X(n)X^T(n) = \int_{(n-1)T_f}^{nT_f} r(t) P_G(\tilde{\tau}) dt \int_{(n-1)T_f}^{nT_f} r(t) P_G{}^T(\tilde{\tau}) dt$$

$$= \int_{(n-1)T_f}^{nT_f} r^2(t) \int_{(n-1)T_f}^{nT_f} P_G(\tilde{\tau}) P_G{}^T(\tilde{\tau}) dt dt$$

$$= \int_0^{T_f} r^2(t) \begin{bmatrix} \int_0^{T_f} p_g^2(t-\tilde{\tau}_1) dt & \cdots & 0 \\ \vdots & \ddots & \vdots \\ 0 & \cdots & \int_0^{T_f} p_g^2(t-\tilde{\tau}_{L_p}) dt \end{bmatrix} dt$$

$$= \begin{bmatrix} R(0) & \cdots & 0 \\ \vdots & \ddots & \vdots \\ 0 & \cdots & R(0) \end{bmatrix} \int_0^{T_f} r^2(t) dt \qquad (5.44)$$

where $R(0) = \int_0^{T_f} p_g^2(t) dt$. From channel model (5.40) and received signal model

(5.41), we could conclude that

$$\int_0^{T_f} r^2(t)dt = R(0) + \frac{N_0}{2}T_f \tag{5.45}$$

Then, we should deal with the 2nd term in (4.18)

$$X(n)d(n) = \left(\left\langle \Gamma \cdot R_{L_p\times 1}(\tau-\tilde{\tau})\right\rangle + a_n\int_0^{T_f} n(t)P_G(\tilde{\tau})dt\right)R(0), \tag{5.46}$$

where $R_{L_p\times 1}(\tau-\tilde{\tau}) = \left[\int_0^{T_f} p_g(t-\tau_1)p_g(t-\tilde{\tau}_1)dt, \quad \cdots \quad , \int_0^{T_f} p_g(t-\tau_{L_p})p_g(t-\tilde{\tau}_{L_p})dt\right]^T$,

and $\left\langle \vec{\alpha}\cdot\vec{\beta}\right\rangle$ is the inner product of vectors $\vec{\alpha}$ and $\vec{\beta}$.

Substituting (5.44) to (5.46) into (4.18), the RAKE coefficient of the i^{th} finger is

$$\tilde{\gamma}_i = \frac{\gamma_i\int_0^{T_f} p_g(t-\tau_i)p_g(t-\tilde{\tau}_i)dt + a_n\int_0^{T_f} n(t)p_g(t-\tilde{\tau}_i)dt}{R(0)+\frac{N_0}{2}T_f}. \tag{5.47}$$

For $i\in[1, L_c]$, i.e. correctly detected the path delay, $\tau_i = \tilde{\tau}_i$, (5.47) becomes

$$\tilde{\gamma}_i = \frac{R(0)}{R(0)+\frac{N_0}{2}T_f}\gamma_i + \frac{a_n n_i(t)}{R(0)+\frac{N_0}{2}T_f} \tag{5.48}$$

where $n_i(t) = \int_0^{T_f} n(t)p_g(t-\tilde{\tau}_i)dt$ is the AWGN after correlation at the i^{th} branch. The distribution of $n_i(t)$ is easily derived as $n_i(t) \sim N\left(0, R(0)\cdot {}^{N_0}\!/_{2}\right)$. Note for high SNR, (5.48) reduces to a more simplified formula,

$$\tilde{\gamma}_i = \gamma_i + \frac{a_n n_i(t)}{R(0)+\frac{N_0}{2}T_f}. \tag{5.49}$$

For $i\in[L_e, L_p]$, i.e. incorrectly detecting the path delay, $\tau_i \neq \tilde{\tau}_i$, with the assumption that $\int_0^{T_f} p_g(t-\tau_i)p_g(t-\tilde{\tau}_j)dt = 0, \ for\ \tau_i \neq \tilde{\tau}_j$, (5.47) becomes

$$\tilde{\gamma}_i = \frac{a_n n_i(t)}{R(0)+\frac{N_0}{2}T_f}. \tag{5.50}$$

Refer back to equation (4.12), only L_c out of L_p paths are synchronized,

$$\tilde{\tau}=\Big[\underbrace{\tilde{\tau}_0,\tilde{\tau}_1,\cdots,\tilde{\tau}_{L_c-1}}_{\left|\leftarrow\cdots L_c\cdots\rightarrow\right|},\underbrace{\tilde{\tau}_{L_c},\cdots,\tilde{\tau}_{L_p-1}}_{\left|\leftarrow\cdots L_e\cdots\rightarrow\right|}\Big]^T . \tag{5.51}$$

RAKE output (5.43) becomes

$$y(n)=a_n\sum_{i=0}^{L_c-1}\gamma_i\tilde{\gamma}_i\int_0^{T_f}p_g(t-\tau_i)p_g(t-\tilde{\tau}_i)dt+\sum_{i=0}^{L_p-1}\tilde{\gamma}_i\int_0^{T_f}n(t)p_g(t-\tilde{\tau}_i)dt$$

$$=a_n\sum_{i=0}^{L_c-1}\gamma_i\left(\gamma_i+\frac{a_n n_i(t)}{R(0)+\frac{N_0}{2}T_f}\right)R(0)+\sum_{i=0}^{L_c-1}\left(\gamma_i+\frac{a_n n_i(t)}{R(0)+\frac{N_0}{2}T_f}\right)n_i(t)+a_n\sum_{i=L_c}^{L_p-1}\frac{n_i(t)n_i(t)}{R(0)+\frac{N_0}{2}T_f}$$

$$=a_nR(0)\sum_{i=0}^{L_c-1}\gamma_i\gamma_i+\frac{a_n^2R(0)}{R(0)+\frac{N_0}{2}T_f}\sum_{i=0}^{L_c-1}\gamma_i n_i(t)+\sum_{i=0}^{L_c-1}\gamma_i n_i(t)+a_n\sum_{i=0}^{L_p-1}\frac{n_i(t)n_i(t)}{R(0)+\frac{N_0}{2}T_f}$$

$$=a_nR(0)\sum_{i=0}^{L_c-1}\gamma_i\gamma_i+\left(\frac{R(0)}{R(0)+\frac{N_0}{2}T_f}+1\right)\sum_{i=0}^{L_c-1}\gamma_i n_i(t)+a_n\sum_{i=0}^{L_p-1}\frac{n_i(t)n_i(t)}{R(0)+\frac{N_0}{2}T_f} . \tag{5.52}$$

For $a_n=+1$

$$y(n)\,|_{a_n=+1}=R(0)\sum_{i=0}^{L_c-1}\gamma_i^2+\frac{2\zeta_0+1}{\zeta_0+1}\sum_{i=0}^{L_c-1}\gamma_i n_i(t)+\frac{1}{R(0)+\frac{N_0}{2}T_f}\sum_{i=0}^{L_p-1}n_i^2(t)\ , \tag{5.53}$$

And for $a_n=-1$

$$y(n)\,|_{a_i=-1}=-R(0)\sum_{i=0}^{L_c-1}\gamma_i^2+\frac{2\zeta_0+1}{\zeta_0+1}\sum_{i=0}^{L_c-1}\gamma_i n_i(t)-\frac{1}{R(0)+\frac{N_0}{2}T_f}\sum_{i=0}^{L_p-1}n_i^2(t)\ , \tag{5.54}$$

where $\zeta_0=\dfrac{2R(0)}{N_0T_f}$.

The decision rule is simply

$$y(n)\ \underset{a_n=-1}{\overset{a_n=+1}{\gtrless}}\ 0 . \tag{5.55}$$

The error probability is $P_e=P(y(n)<0\,|\,a_n=+1)$ (the PDF is symmetric for $a_n=\pm1$). Since the last term in (5.53) will never be a negative value, it will never affect the error performance of the RAKE receiver. It is negligible when analyzing the

RAKE performance. For high SNR,

$$y(n)\,|_{a_n=+1} = R(0)\sum_{i=0}^{L_c-1}\gamma_i^2 + 2\sum_{i=0}^{L_c-1}\gamma_i n_i(t) \tag{5.56}$$

Fixing the fading coefficients γ_i, the instantaneous SNR of equation (5.56) is

$$\zeta = \zeta_0 \frac{\sum_{i=0}^{L_c-1}\gamma_i^2}{4} \tag{5.57}$$

where $\zeta_0 = \dfrac{2R(0)}{T_f N_0}$ is the AWGN signal SNR. Since γ_i's are lognormal distributed R.V.s, it is not difficult to see the truth that γ_i^2 are also lognormal R.V.s, and $\ln \gamma_i^2$ is a Gaussian distributed R.V. with mean $\mu_{\gamma^2} = 2\mu_\gamma$, and $\sigma_{\gamma^2} = 2\sigma_\gamma$. Thus, according to [29], and [2], the error probability is

$$p_e(L_c) = \int_0^\infty Q(\sqrt{\zeta})\, f(\zeta)\, d\zeta \tag{5.58}$$

where $f(\zeta)$ is the distribution of the lognormal squared summation of equation (5.57), ζ is a square summation of i.i.d. lognormal R.V.s. The analytical solution of $f(\zeta)$ is a long standing problem in wireless communications. The characteristic function of a lognormal R.V. is not known and is very difficult to compute, even for a numerical solution because of its slow decaying rate of the tail of a lognormal PDF [30]. A variety of asymptotic approaches has been proposed [22], [23], [29], [30]. They diverge into two approaches. The first is to approximate the sum of independent lognormal R.V.s by another lognormal R.V. [22], [23], [29]. Another approach tries to find a dedicatedly constructed closed-form equation to approximate the target [30]. Among them, two possible candidates are highlighted in this thesis. A lognormal approximation is proposed [29]

$$f(x) = \frac{1}{x\sqrt{2\pi\sigma_z^2}} \exp\left[-\frac{(\ln(x) - \mu_z)^2}{2\sigma_z^2} \right], \tag{5.59}$$

where μ_z and σ_z are calculated with the known parameters of the i.i.d. R.V. Another option is a highly accurate and simple closed-form approximation [30]

$$f(x) = \frac{a_1 a_2}{\sqrt{2\pi}} \exp\left(-\frac{1}{2}\left(a_0 - a_1 e^{-x a_2}\right)^2 - x\left(a_2 + \lambda\right) \right), \quad (5.60)$$

where $\lambda = \ln 10/10$, and other parameters a_0, a_1, a_2 are chosen depending on different values of N and σ which are the length of summation and dB spread for lognormal R.V. respectively [30]. Some of the optimum values have already been tabulated. The cumulative density function (CDF) is simply [30]

$$F(x) = a_0 - a_1 e^{-a_2 x}. \quad (5.61)$$

Equation (5.58) is the error probability of a RAKE with L_c fingers correctly synchronized. Each finger synchronized with a detection probability

$$P_d(\zeta_0, \lambda) = \int_{\lambda}^{+\infty} f_{X_{fa}|H_1}\left(x_{fa}\right) d\lambda, \quad (5.62)$$

where $f_{X_{fa}|H_1}\left(x_{fa}\right)$ is the PDF (see equation (5.36)), λ is the threshold value, and a false alarm rate of $P_{fa}(\lambda)$ which is irrelevant to input SNR ζ_0. And the probability for the event that L_c out of L_p paths are correctly synchronized is

$$P(L_c) = \begin{pmatrix} L_p \\ L_c \end{pmatrix} P_d^{L_c}(\zeta_0, \lambda) \cdot P_{fa}^{L_p - L_c}(\lambda), \quad (5.63)$$

where ζ_0 is the input SNR, $P_d(\zeta, \lambda)$ is the detection probability (5.38) and $P_{fa}(\lambda)$ is the false alarm probability (5.39) of the proposed synchronization scheme. The average performance of the proposed RAKE receiver is a weighted sum of all possible $P(L_c)$ with different L_c values,

$$P_e = \sum_{l=0}^{L_p} p_e(l) \cdot P(l), \quad (5.64)$$

where $p_e(l)$ is from (5.58) and $P(l)$ is from (5.63).

The equation (5.64) is suitable for all the performance analysis of imperfectly synchronized RAKE receiver. The interpretation of (5.64) is as follows. Assume a L_p fingers RAKE receiver, the event l out of L_p fingers synchronize correctly and other $L_p - l$ fingers fail is occurred with the probability of $P(l)$. The error performance $p_e(l)$ is the receiver performance when l fingers out of total L_p fingers are synchronized. Thus the average performance is the weighted summation for the cases from $l = 0$ fingers is synchronized to $l = L_p$ fingers are synchronized.

The T&L synchronization based RAKE outperforms other RAKE because the synchronization algorithm for each branch is superior to other conventional algorithms as what have been proven in the previous sections. For each L_c, as long as $P(L_c)|_{T\&L}$ outperforms $P(L_c)|_{ML}$, $P_e|_{T\&L}$ outperforms $P_e|_{ML}$.

6 SIMULATION RESULTS

6.1 Comparison of Matched Filter (MF) based Detector Performance and Proposed Detector under AWGN channel

6.1.1 MF Based Detector Performance

Performance simulation was carried out to verify the performance analysis of the proposed synchronization scheme. Since the synchronization to different branches were all the same, the simulation was carried out with regard to only one path with fixed path coefficient, and different SNR to test the detector performance under different circumstance.

Typical simulation setting are 2nd order Gaussian monocycle with 0.25ns pulse width. The correlation output SNR is at 5, 10, and 15dB. The pulse repetition rate is set at 100Mbps which indicates 10ns frame length. Thus the processing gain is, theoretically, as equation (5.8), approximately 15dB. This makes an UWB system outperforms a conventional communication system with the same signal energy.

200×10^6 data were recorded for each SNR, among them 2×10^6 data points were categorized as H_1, and the remains were otherwise.

The simulation results (solid line and labeled with marks) were depicted graphically in the same plot against the theoretic results (dash dot line and without marks). Approximately 15dB gain was observed as predicted by equation (5.8). The simulation results were consistent with the theoretic one. The theoretic counterpart of Figure 6.1 is Figure 5.2. All the SNR values on Figure 6.1 are correlation output SNR.

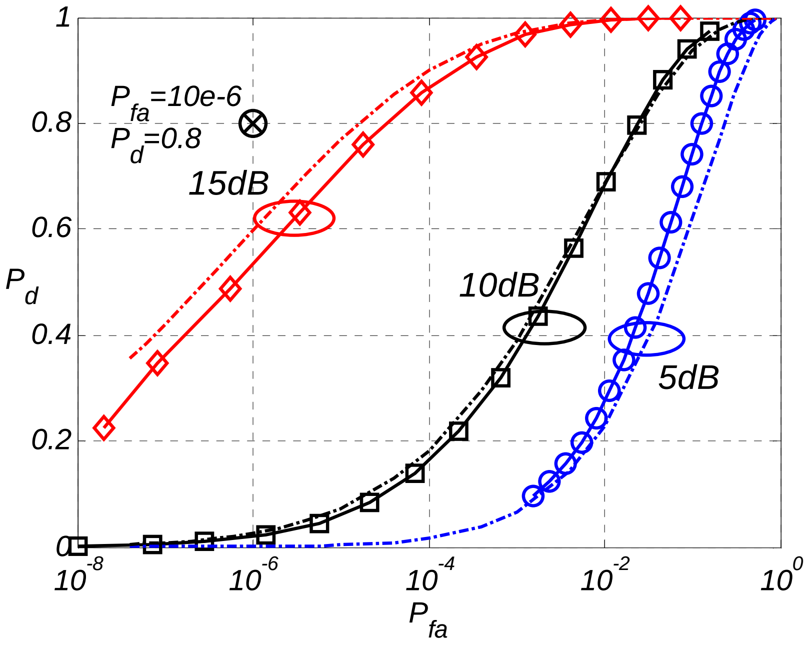

Figure 6.1 Simulation Results of ML Based Detector Performance vs. Theoretic One.

6.1.2 T&L Based Detector Performance

The simulation for T&L based synchronization scheme is carried out with following settings. The SNR is chosen to be the SNR after the correlation, i.e. including the processing gain. And the processing gain, according to the simulation observation in the previous section, is approximately 15dB. The forgetting factor ρ is 0.04. SNR value covers all typical range from 5dB to 15dB. 25×10^6 data were accumulated, among them 2.5×10^6 data were categorized as the H_1 subset.

The simulation results are depicted in Figure 6.2. Several conclusions are derived. At high SNR, e.g. 10dB and 15dB, the theoretic curves were consistent with the simulation curves precisely. While at low SNR, e.g. 0dB and 5dB, although a slight deviation was presented, the simulation results generally complied with the theoretic analysis.

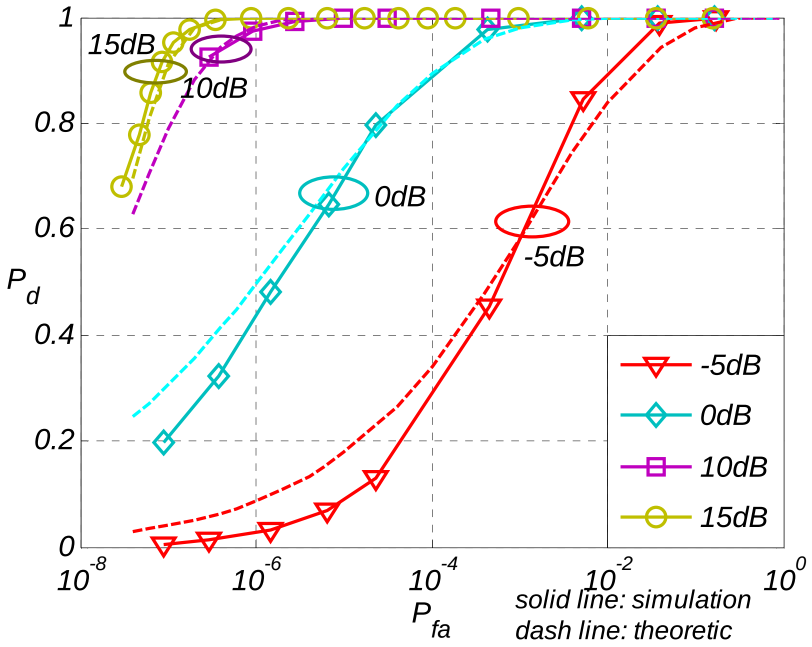

Figure 6.2 Simulation Results of T&L Based Detector Performance vs. Theoretic One.

6.2 Proposed Detector Performance under Modified S-V Channel Model

Although the superiority of the proposed synchronization algorithm could be concluded from the analysis and simulation under a fixed path coefficient, the performance under practical channel is still of great interests. Practically, a receiver is supposed to find the beginning of a frame first, usually, this indicates to find the line-of-sight (LOS) path. The received signal model is depicted in equation (5.35). The signal component is subject to a log-normal attenuation.

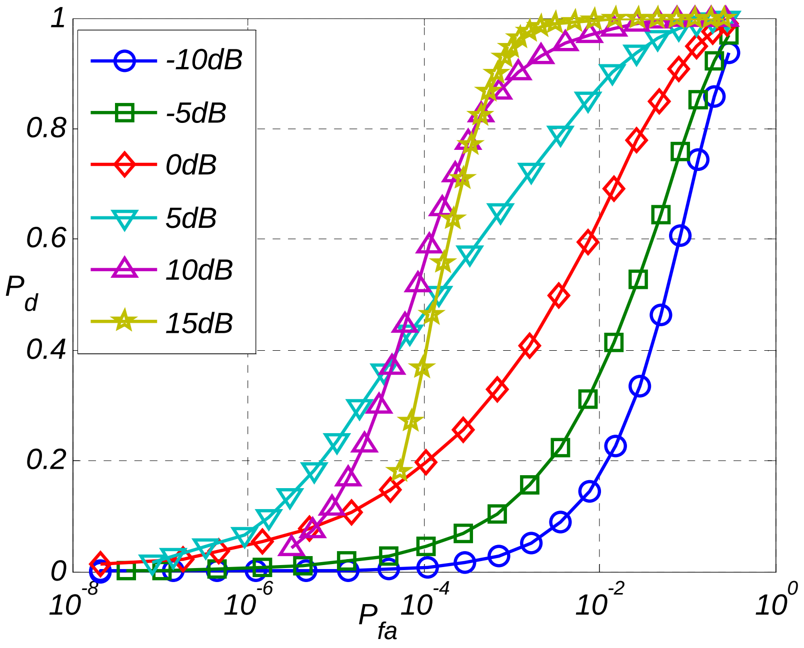

Figure 6.3 Simulation Results of T&L Based Detector Performance for LOS Detection.

Simulation was carried out with typical settings. The SNR range covered all possible values from -10dB to 15dB after the correlation receiver. The forgetting factor ρ was 0.04. 200×10^6 data is observed, among which 20×10^6 were categorized as H_1.

Comparing Figure 6.3 to Figure 6.2, performance degradation was observed due to the varying fading coefficient. Figure 6.3 is a more practical curve which is a good guideline when predicting synchronization performance of RAKE fingers.

7 HARDWARE IMPLEMENTATION

7.1 Hardware System Architecture

The target of this project is to develop a high performance and effective synchronization algorithm for IR UWB systems. To verify the proposed algorithm, the MATLAB algorithm is first converted to Verilog coding. Behavior level simulation results of the Verilog coding was depicted in Figure 7.1. The simulation results were consistent with the MATLAB simulation.

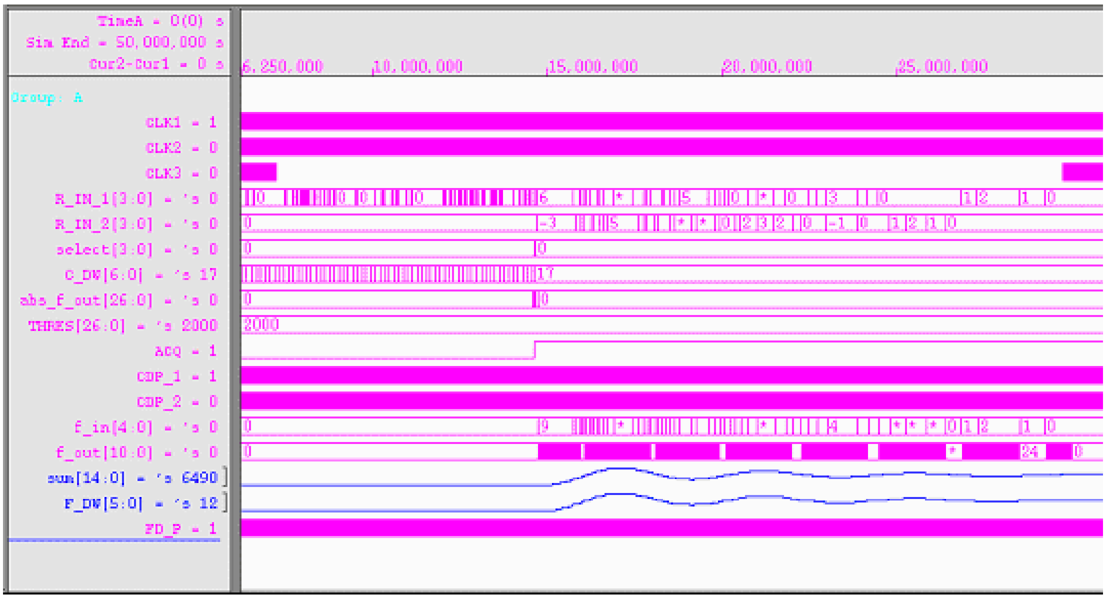

Figure 7.1 Behavior Level Simulation Results of Verilog Coding.

The proposed synchronization algorithm was implemented on a Xilinx Virtex IV Pro FPGA to verify the functionality. Due to some of the hardware limitation, for example the speed of the FPGA, the algorithm was working at a reduced rate which was 5MHz. The data after correlation were previously generated by computer simulation. A logic analyzer was connected to the FPGA to monitor the status of the algorithm. The output of the timing delay value was captured and compared with simulation results. The behaviors of these two are consistent with each other.

7.2 Hardware Simulation Results

By printing the display of the logic analyzer and monitoring the digital position output, the functionality is verified. A typical testing result captured from a logic analyzer display was shown in Figure 7.2.

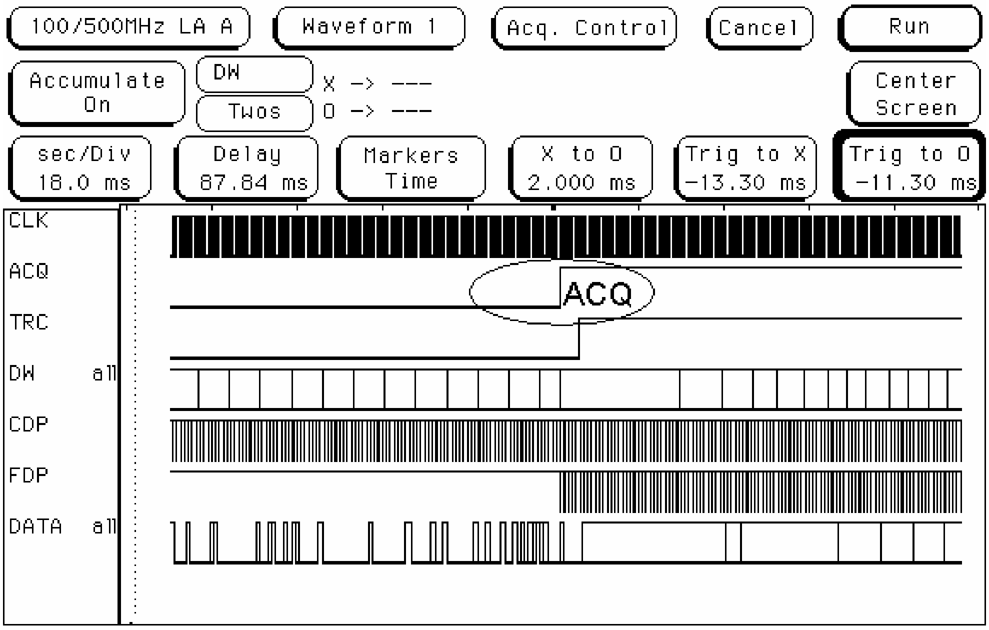

X -> ---
O -> ---
sec/Div 18.0 ms
Delay 87.84 ms
X to O 2.000 ms
Trig to X -13.30 ms
Trig to O -11.30 ms

Figure 7.2 Logic Analyzer Output When Acquisition is Achieved.

The delay word (DW) was the output of the synchronization scheme. Coarse delay pulse (CDP) and fine delay pulse (FDP) were square waves which triggered the local UWB pulse at their rising edges. The delay value of CDP and FDP were controlled by DW. The input data (DATA) was a randomized sequence. The synchronization scheme started with the acquisition mode during which the ACQ signal was set low. As soon as acquisition is claimed, ACQ signal was set high. CDP delay was consequently frozen. After the TRC signal was set high, the synchronization scheme preceded to the tracking mode several clock cycles later. The tracking loop output drove the FDP back and forth to find the equilibrium point. These results change were all reflected from the value of DW. The hardware testing results once again verified that the proposed synchronization algorithm works well in practical implementation.

8 CONCLUSION

In this thesis, a new CFAR detector for impulse UWB synchronization is proposed. The theoretic performance analysis is closed by giving the ROC curves which are compared with the conventional MF based detectors. The performance analysis shows great advantage by employing this proposed detector. Other than increasing SNR which is the traditional method when the receiver ROC could not meet the requirements, the forgetting factor ρ of the proposed detector enables the designer more flexibility and control over the system performance. By adjusting ρ, the ROC at a certain SNR could be altered. When choosing ρ less than 0.04, the proposed detector outperforms conventional MF based detectors with the same SNR input. Intensive simulation were also carried out to verify the theoretic analysis and compared with the numerical results. Precise match between theoretic performance analysis and simulation results were observed.

The RAKE receiver based on the proposed synchronization was also constructed and analyzed theoretically. The performance analysis shows that the proposed detector is superior to the conventional method. The RAKE receiver based on proposed synchronization scheme outperforms the traditional ones.

Finally the hardware implementation results were also presented in the last chapter.

REFERENCES

[1] http://ieee802.org/11/

[2] J. G. Proakis, *Digital Communication*, 4th edition, New York: McGraw-Hill, 2001.

[3] G. F. Ross, “The transient analysis of certain TEM mode four-post networks”, *IEEE Trans. Microwave Theory Techno.*, vol.14, pp.528, Nov. 1966.

[4] Moe Z. Win and R. A. Scholtz, “Characterization of Ultra-Wide Bandwidth Wireless Indoor Channels: A Communication-Theoretic View”, *IEEE Journal on Selected Areas in Communications*, vol.20, no. 9, pp.1613-1627, Dec. 2002.

[5] “Assessment of Ultra-Wideband (UWB) Technology”, OSD/DARPA Ultra-Wideband Radar Review Panel, R-6280, Defense Advanced Research Projects Agency (July 13, 1990).

[6] R. L. Peterson, R. E. Ziemer, and D. E. Borth, *Introduction to Spread-Spectrum Communications*, Prentice Hall, Englewood Cliffs, NJ.

[7] L. Zhao and A. M. Haimovich, “Performance of Ultra-Wideband Communications in the Presence of Interference,” *IEEE Journal on Selected Areas in Communications*, vol. 20, no. 9, pp. 1684-1691, Dec. 2002.

[8] Liuqing Yang and Georgios B. Giannakis, “Ultra-Wideband Communications: An Idea Whose Time Has Come”, *IEEE Signal Processing Magazine*, vol.21, Issue 6, pp. 26–54, Nov. 2004.

[9] Stephan V. Schell, “Analysis of Time Variance of a UWB Propagation Channel”, *IEEE P802.15-02/452-SG3a and IEEE P802.15-02/453-SG3a*.

[10] J. Foerster, “Wireless Personal Area Networks: Channel Modeling Sub-committee Report Final,” *IEEE P802.15-02/368r5-SG3a, Oct. 2003.*

[11] Chee-Cheon Chui and R. A. Scholtz, “Tracking UWB Monocycles in IEEE 802.15 Multi-path Channels”, in Proc. *2003. IEEE Conference Record of the Thirty-Seventh Asilomar Conference on, Signals, Systems and Computers* vol.2, pp.1761–1765, 9-12 Nov. 2003.

[12] Chee-Cheon Chui and R.A. Scholtz, “Optimizing Tracking loop for UWB Monocycles”, in Proc. *IEEE Global Telecommunications Conference, 2003. (GLOBECOM '03).* vol.1, pp.425-430, 1-5 Dec. 2003.

[13] L. Yang and G.B. Giannakis, “Blind UWB timing with a dirty template”, in Proc. *Int. Conf. Acoustics, Speech, and Signal Processing*, Montreal, Quebec, Canada, pp.509-512，2004.

[14] W. S. Ho, X. M. Peng, A. S. Madhukumar, and F. Chin, “Rapid Acquisition for Multiband UWB Systems: CAZAC vs. Barker Sequences,” in Proc. *ICICS-PCM 2003,* Dec. 2003.

[15] Steven M.Kay, *Fundamentals of Statistical Signal Processing: Volume II Detection Theory*, Prentice Hall, NJ, USA, 1998.

[16] D. W. Trigg and A. G. Leach, “Exponential smoothing with an adaptive response rate,” *Operation Research*, vol. 18, pp.53-59, 1967.

[17] B. Carlsson, “Digital differentiating filters and modeal based fault detection,” Ph.D. dissertation, Dept. Automation Control, Uppsala Univ., Uppsala, Sweden, 1989.

[18] Yuanjin Zheng, Zhiping Lin, “Recursive Adaptive Algorithms for Fast Rapidly Time- Varying Systems,” *IEEE Trans. on Circuits and Systems-II*, vol. 50, no. 9, pp.602-614, Sept. 2003.

[19] Zhi Tian and Vincenzo Lottici, “Efficient timing acquisition in dense multipath for UWB communications”, in Proc. *IEEE 58th Vehicular Technology Conference, 2003.*, vol.2., pp.1318-1322, 6-9 Oct. 2003.

[20] Stefan Franz and Urbashi Mitra, “On Optimal Data Detection for UWB Transmitted Reference Systems”, in Proc. *Global Telecommunications Conference, 2003. GLOBECOM '03. IEEE*, vol.2, pp. 744-748, 1-5 Dec. 2003.

[21] M. Z. Win and R. A. Scholtz, “Energy Capture vs. Correlator Resources in Ultra-Wide Bandwidth Indoor Wireless Communications Channels”, in Proc. *MILCOM 97*, Vol.3, pp. 1277-1281, 2-5 Nov. 1997.

[22] Huaping Liu, “Error Performance of a Pulse Amplitude and Position Modulated Ultra-Wideband system over Lognormal Fading Channels”, *Communications Letters, IEEE,* vol.7, pp. 531-533, Issue 11, Nov. 2003.

[23] Huaning Niu, James A. Ritcey and Hui Liu, “Performance of UWB RAKE Receivers with Imperfect Tap Weights”, in Proc. *2003 IEEE International Conference on, Acoustics, Speech, and Signal Processing, 2003. (ICASSP '03).* vol.4, pp. IV - 125-8, 6-10 April 2003.

[24] Vincenzo Lottici, Aldo D’Andrea, and Umberto Mengali, “Channel Estimation for Ultra-Wideband Communications”, *IEEE Journal on Selected Areas in Communications*, vol. 20, NO.9, pp.1638-1646, Dec.2002.

[25] S. Hykin, *Adaptive Filter Theory*, 4th Edition, Prentice Hall, NJ, USA 2002.

[26] B. Farhang Boroujeny, *Adaptive Filters-Theory and Applications*, John Wiley & Sons, West Sussex, UK 1998.

[27] Arjunan Rajeswaran, V.Srinivasa Somayazulu, Jeffrey R. Foerster, “RAKE Performance for A Pulse Based UWB System in a Realistic UWB Indoor Channel”, in Prof. *IEEE International Conference on, Communications, 2003. ICC '03.* vol.4, pp. 2879-2883, 11-15 May 2003.

[28] A. Papoulis and S. U. Pillai, *Probability, Random Variables and Stochastic Processes,* McGraw-Hill, 2002.

[29] Huaping Liu, “error performance of a pulse amplitude and position modulated ultra-wideband system over lognormal fading channel”, *Communications Letters, IEEE,* vol.7, Issue 11, pp. 531-533, Nov. 2003.

[30] Norman C. Beaulieu, and Faruq Rajwani, “Highly Accurate Simple Closed-Form Approximations to Lognormal Sum Distributions and Densities”, *Communications Letters, IEEE,* vol.8, NO.12, Dec.2004.

[31] Petriu, E.M.; Basran, J.S.; “On the position measurement of automated guided vehicles using pseudorandom encoding”, *Instrumentation and Measurement, IEEE Transactions on,* vol. 38, Issue 3, pp. 799-803, June 1989.

[32] Mau-Lin Wu, Kuei-Ann Wen, Chao-Wang Haung, “Efficient pseudonoise code design for spread spectrum wireless communication systems”, *IEEE Trans. On, Circuits and Systems II: Analog and Digital Signal Processing,* vol. 48, Issue 6, pp.606-613, June 2001.

[33] Sankaran, C., Ephremides, A. “Solving a class of optimum multiuser detection problems with polynomial complexity”, *Information Theory, IEEE Trans. on,* vol. 44, Issue 5, pp.1958-1961, Sept. 1998.

[34] Denic', D., Arsic', M., “Checking of pseudorandom code reading correctness”, *Electronics Letters,* vol. 29, Issue 21, pp.1843-1844, 14 Oct. 1993.

[35] Cruselles, E., Soriano, M., Melus, J. L., “Uncorrelated PN sequences generator for spreading codes in CDMA systems”, in Proc. *Personal, Indoor and Mobile Radio Communications, 1995. PIMRC'95. 'Wireless: Merging onto the Information Superhighway'., Sixth IEEE International Symposium on,* vol. 3, pp.1335, 27-29 Sept. 1995.

[36] Zhendong Luo, Hong Gao, Yuanan Liu, Jinchun Gao, “A new UWB pulse design method for narrowband interference suppression”, in Proc. *Global Telecommunications Conference, 2004. GLOBECOM '04. IEEE,* vol. 6, pp. 3488-3492, 29 Nov.-3 Dec.2004.

[37] Seaman, R.L., Jauchem, J.R., “Rat electrocardiogram during acute exposure to synchronized bursts of ultra-wideband pulses”, *Plasma Science, IEEE Trans. on,* vol.32, Issue 4, pp. 1644 -1652, Aug. 2004.

[38] Miller, L.E., “Models for UWB pulses and their effects on narrowband direct conversion

receivers", in Proc. *Ultra Wideband Systems and Technologies, 2003 IEEE Conference on,* pp. 101-105, 16-19 Nov. 2003.

[39] Camp, M., Garbe, H., Nitsch, D., "Influence of the technology on the destruction effects of semiconductors by impact of EMP and UWB pulses", in Proc. *2002 IEEE International Symposium on, Electromagnetic Compatibility,* vol.1, pp. 87-92, 19-23 Aug. 2002.

[40] Parr, A.B., Cho, B.L., Ding, Z., "A new UWB pulse generator for FCC spectral masks", in Proc. *The 57th IEEE Semiannual, Vehicular Technology Conference, 2003. VTC 2003-Spring.* vol. 3, pp. 1664-1666, 22-25 April 2003.

[41] Yun Hwa Choi, "Gated UWB pulse signal generation", in Proc. *Ultra Wideband Systems, 2004. Joint with Conference on Ultra-wideband Systems and Technologies. Joint UWBST & IWUWBS.* pp.122-124, 18-21 May 2004.

[42] Aedudodla, S., Vijayakumaran, S., Wong, T.F., "Rapid ultra-wideband signal acquisition", in Proc. *Wireless Communications and Networking Conference, 2004. WCNC. 2004 IEEE,* vol. 2, pp. 1148-1153, 21-25 March 2004.

[43] S.Ghassemzadeh, V.Tarokh, "The Ultra-Wideband Indoor Path Loss Model", *IEEE P802.15-02/277-SG3a and IEEE P802.15-02/278-SG3a.*

[44] M. Pendergrass, "Empirically Based Statistical Ultra-Wideband Channel Modle", *IEEE P802.15-02/240-SG3a.*

[45] J. Foerster and Q. Li, "UWB Channel Modeling Contribution from Intel", *IEEE P802.15-02/279-SG3a.*

[46] G. Shor, et. Al., "A proposal for a selection of indoor UWB path loss model", *IEEE P802.15-02/280-SG3a.*

[47] J. Kunisch and J. Pamp, "Radio Channel Model for Indoor UWB WPAN Environments", *IEEE P802.15-02/281-SG3a.*

[48] S. Ghassemzadeh and V. Tarokh, "The Ultra-Wideband Indoor Multipath Loss Model", *IEEE P802.15-02/282-SG3a and IEEE P802.15-02/283-SG3a.*

[49] J-M Cramer, R. Scholtz, M. Win, "Evaluation of an Indoor Ultra-Wideband Propagation Channel", *IEEE P802.15-02/286-SG3a and IEEE P802.15-02/325-SG3a.*

[50] Emami, S., Corral, C., Rasor, G., "Peak-to-average power ratio (PAPR), fractional bandwidth and processing gain of UWB schemes", *IEEE Eighth International Symposium on, Spread Spectrum Techniques and Applications, 2004.* pp.929-933, 30 Aug.-2 Sept. 2004.

[51] Sadler, B.M., Swami, A., “On the performance of UWB and DS-spread spectrum communication systems”, in Proc. *2002 IEEE Conference on*, *Ultra Wideband Systems and Technologies, 2002. Digest of Papers.* pp. 289-292, 21-23 May 2002.

[52] Somayazulu, V. S., Foerster, J. R., Roy, S., “Design challenges for very high data rate UWB systems”, in Proc. *Signals, Systems and Computers, 2002. Conference Record of the Thirty-Sixth Asilomar Conference on*, vol.1, pp. 717-721, 3-6 Nov. 2002.

[53] Gonzalez, O.V., Moreno, W.A., “Narrowband interference detection in multiband UWB systems”, *2005 IEEE/Sarnoff Symposium on*, *Advances in Wired and Wireless Communication*, pp. 160-163, April 18-19, 2005.

[54] Siriwongpairat, W. P., Weifeng Su, Olfat, M., Liu, K.J.R., “Space-time-frequency coded multiband UWB communication systems”, in Proc. *Wireless Communications and Networking Conference, 2005 IEEE*, vol.1, pp. 426-431, 13-17 March 2005.

[55] C. L. Bennett and G. F. Ross, “Time-domain electromagnetics and its applications”, *in Proc of the IEEE*, vol. 66, pp.299-318, Mar. 1978.

LIST OF PUBLICATIONS

[1] Y. J. Zheng, R. Cao, and Y. Lian, “A New Synchronization Algorithm for UWB Impulse Radio Communication Systems”, in Proc. *IEEE, 9th International Conference on Communication Systems,* pp.25-pp.29. Sept. 2004

[2] R. Cao, Y. J. Zheng, and Y. Lian, “A CFRA Synchronization Scheme for Impulse Based UWB Receiver”, paper accepted by ISCAS 2006.